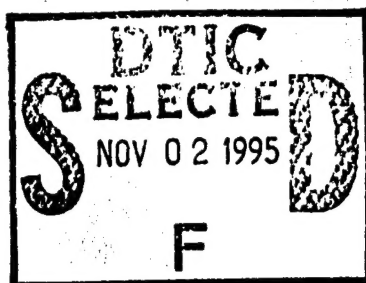


NASA  
Technical  
Paper  
3567

ATCOM  
Technical  
Report  
95-A-004

1995



# ZETA II Code for Determining the Flow Around Multielement and Deformable Airfoils

C. M. Wang, J. C. Wu, K. W. McAlister, and C. Tung

DISTRIBUTION STATEMENT A  
Approved for public release  
Distribution Unlimited

19951030 078

DTIC QUALITY INSPECTED 5



National Aeronautics and  
Space Administration



US Army  
Aviation and Troop Command

Aeroflughtdynamics Directorate  
Moffett Field, CA 94035-1000

**NASA  
Technical  
Paper  
3567**

**ATCOM  
Technical  
Report  
95-A-004**

1995

**ZETA II Code for Determining the  
Flow Around Multielement and  
Deformable Airfoils**

C. M. Wang and J. C. Wu

*School of Aerospace Engineering, Georgia Institute of Technology,  
Atlanta, Georgia*

K. W. McAlister and C. Tung

*Aeroflightdynamics Directorate, U.S. Army Aviation and Troop Command,  
Ames Research Center, Moffett Field, California*

Accession For	
NTIS	CRA&I
DTIC	TAB
Unannounced	
Justification	
By _____	
Distribution / _____	
Availability Codes	
Dist	Avail and/or Special
A-1	



National Aeronautics and  
Space Administration

**Ames Research Center**  
Moffett Field, CA 94035-1000



US Army  
Aviation and Troop Command

**Aeroflightdynamics Directorate**  
Moffett Field, CA 94035-1000

## TABLE OF CONTENTS

	Page
NOMENCLATURE .....	v
SUMMARY .....	1
INTRODUCTION .....	1
MATHEMATICAL FORMULATIONS .....	3
Conformal Mapping of Two-Element Airfoils .....	4
Kinematics .....	4
Fourier Series Expansion .....	6
Vorticity Integral Constraints .....	9
Kinetics .....	10
NUMERICAL FORMULATIONS .....	11
DYNAMIC STALL .....	13
Slatted Airfoils .....	13
Deformable Airfoils .....	14
VORTEX-AIRFOIL INTERACTIONS .....	15
CONCLUSIONS .....	17
REFERENCES .....	18

## NOMENCLATURE

### Symbols

$\bar{a}$	location of singularity on real axis in $\zeta$ -plane
$B$	boundary of fluid in region $R$
$c$	airfoil chord
$C_d$	drag coefficient
$C_\ell$	lift coefficient
$C_m$	pitching-moment coefficient
$C_p$	surface pressure
$\vec{e}$	unit directional vector in $\zeta$ -plane
$h$	total head
$H$	scale factor of transformation
$k$	reduced frequency, $\Omega c / 2v_\infty$
$\vec{n}$	unit normal vector on $B$ directed outward
$p$	pressure
$\vec{Q}$	gradient of fundamental solution of elliptic equations
$R$	region of fluid between $B$ and $S$
$Re$	Reynolds number, $cv_\infty/\nu$
$S$	solid surface
$t$	time
$\vec{v}$	velocity
$X$	coordinate in physical plane
$Y$	coordinate in physical plane
$z$	complex variable in physical plane
$\alpha$	angle of attack
$\delta$	density of fluid
$\zeta$	complex variable in computational plane
$\Gamma$	circulation
$\nu$	kinematic viscosity
$\rho$	radial coordinate in $\zeta$ -plane
$\phi$	circumferential coordinate in $\zeta$ -plane
$\omega$	vorticity
$\Omega$	oscillation frequency of pitching airfoil

### Subscripts

$G$	grid
$o$	quantity in $\rho_o$ space
$P$	point vortex
$\infty$	free-stream condition

### Superscript

$-$	Fourier coefficient
-----	---------------------

## **Acronyms**

AFDD	Aeroflightdynamics Directorate
BVI	Blade–vortex interaction
HACR	Helicopter active control rotor

# **ZETA II CODE FOR DETERMINING THE FLOW AROUND MULTELEMENT AND DEFORMABLE AIRFOILS**

C. M. Wang,\* J. C. Wu,\* K. W. McAlister, and C. Tung

Aeroflightdynamics Directorate, U.S. Army Aviation and Troop Command, Ames Research Center

## **SUMMARY**

The present NASA–University consortium involves research on the development of an efficient and accurate numerical procedure to treat general, unsteady, viscous flows. Of particular interest in the present work are flows relevant to helicopter rotors. Special efforts are centered on new concepts applied to the rotorblade configuration on the helicopter to improve the rotor aerodynamic characteristics. Among them, airfoil dynamic stall and the aerodynamic noise of vortex–airfoil interactions were extensively studied by using the numerical procedure.

The procedure, based on the formulation of an integral representation of the velocity vector and the vorticity-transport equation, is used to solve incompressible Navier–Stokes flows. ZETA, a computer code developed at Georgia Tech, is used as the basis for the development of an extended computer code, ZETA II. The ZETA code is very efficient in the treatment of single, solid airfoils undergoing arbitrary motions. The extended ZETA II can treat the two-element airfoil, the deformable airfoil, and vortex–airfoil interaction.

New concepts aimed at improving the helicopter maneuverability and susceptibility are studied, including the slatted airfoil and the deformable airfoil. Numerical results obtained by using the ZETA II code show that both slatted and deformable airfoils reduce the dynamic stall and that the deformable airfoil reduces the blade–vortex interaction (BVI) noise.

## **INTRODUCTION**

The development of new-generation helicopters to operate at a much higher performance level than in the past requires advanced design concepts and demonstrations. The new generation of helicopters must perform well, particularly in the areas of nap-of-the-Earth, deep-penetration operations, and air-to-air combat. The technology base needed to meet the requirements of a highly maneuverable, agile, and survivable rotorcraft covers the fields of aerodynamics, acoustics, dynamics, and flight controls. The U.S. Army is extending the currently available technology base in a demonstration program called the helicopter active control rotor (HACR) program. The objectives of the program include increasing maneuverability/agility by 50 percent and reducing the acoustic detection range by 50 percent.

---

\*School of Aerospace Engineering, Georgia Institute of Technology, Atlanta, Georgia.

The most important element of the rotorcraft for providing the lift, control, and speed is the main rotor itself. The rotor is also a major source of acoustically detectable radiation. In order to achieve the capabilities desired in the new-generation helicopters, the main research and development effort here will be placed on the demonstration and effectiveness of new concepts for rotorblade design. In particular, the maneuvering capability can be improved by reducing or suppressing the vibratory loads on the rotorblades caused by flow separation and dynamic stall. Suppressing dynamic stall would expand the stall-limiting boundary of the rotor, thereby increasing the available load factor in certain flight maneuvers. The vibratory loads of the rotor are caused by the angle-of-attack change of the blade, which results in a small angle on the advancing side and a large angle on the retreating side. During a dash or a rapid maneuver, the rotorblades often encounter stall on the retreating side, which causes a rapid loss in lift and a sudden increase in both drag and pitching moment.

The impulsive noise generated by the rotor comes from two main sources: the compressible effect near the blade tip and the blade-vortex interaction (BVI) in descending or maneuvering flight. The BVI noise is most critical near the leading edge of a blade when the vortex trajectory is nearly parallel to the blade span. The strong effect of the passing vortex is manifested by a large fluctuation of the surface pressure as the vortex passes close to the leading edge. This large fluctuation is the source of BVI noise.

The requirement for improved maneuverability and reduced susceptibility clearly demands a substantial growth in technologies that address rotor aerodynamics. New passive- and active-control concepts that have the potential to meet the new requirements must be considered with a more thorough physical understanding of the flow phenomena described earlier. Substantially improved prediction capabilities are key elements to providing an understanding of these flow phenomena and to predicting the aerodynamic loads. Various concepts for improving rotor aerodynamic characteristics, including airfoils with a slat or a slot, airfoils with flow energizers, and airfoils that deform, have been proposed by U.S. Army Aeroflightdynamics Directorate (AFDD) researchers.

The main objective of the present study is to demonstrate the effectiveness of some of these new concepts in reducing dynamic stall and BVI noise. In order to do this, efforts are placed on the development of a computer code that can efficiently predict flow phenomena and aerodynamic loads. These flow problems are directly related to the implementation of the new concepts. Georgia Tech researchers have developed a computer code, ZETA, that can predict complex flow phenomena of airfoils undergoing arbitrary motion. The code predicts airfoil load hysteresis loops of dynamic stall to a degree that matches the available experimental data within the experimental error band. The code is based on a vorticity-velocity formulation and an integral formulation for the velocity vector. The efficiency of the code is attributable to the confinement of the computation to the vortical region only. The large potential region surrounding the vortical region does not enter into the computation procedure. For problems of practical interest, the size of the vortical region is much smaller than the size of the potential region.

Furthermore, the vortical region can be partitioned into attached- and detached-flow zones. In the attached-flow zones, the flow is attached to all solid surfaces, and the customary boundary layer approximations are justified. Therefore, the boundary layer equations are solved in these zones. The Navier-Stokes equations are solved in the detached-flow zones, which consist of the separated- and the wake-flow zones. An iterative procedure is required in the detached-flow zones, whereas a simple

marching procedure is used in the attached-flow zones. The marching procedure takes very little time compared to the time consumed for an iterative procedure. The high efficiency of the numerical, zonal method permits an effective way for conducting a parametric study of the new concepts to be implemented on helicopter rotors.

The numerical procedure of the ZETA code is extended in the present effort for treating problems of a broader scope. A numerical, conformal procedure is established first such that two-element airfoil geometries and deformable airfoils can be handled. The conformal-mapping technique is an important element of the present numerical procedure because the conformal mapping leads to the simplest possible form of the governing equations to be solved, and the integral formulation derived for the velocity can be directly used. The ZETA code, developed for solid, single-element airfoils, uses conformal-mapping techniques based on an analytical method. In the extended code ZETA II, conformal mapping is performed numerically so that it can treat two-element and deformable airfoils. The extension from ZETA to ZETA II also includes certain numerical procedures that are made suitable for two-element and deformable airfoils. For BVI problems, a passing vortex is modeled by a single-point vortex that passes close to an airfoil. The high efficiency of the ZETA code is essentially retained in the extended ZETA II code.

Various new concepts for rotorblades are demonstrated by using the newly developed code. In the present study, the slatted airfoil and the deformable airfoil are extensively investigated in order to demonstrate an improvement on dynamic stall and BVI noise.

## MATHEMATICAL FORMULATIONS

Through the introduction of vorticity, a general, unsteady, viscous-flow problem can be partitioned into its kinematic and kinetic aspects. The kinematic aspect describes the velocity field (subject to the velocity boundary condition) corresponding to the vorticity field at any instant of time. The kinetic aspect describes the transport of the vorticity field through convection and diffusion. The vorticity-transport equation is elliptic in space, and, therefore, the vorticity on the flow boundaries is required. The values of vorticity on the solid boundaries, however, are not given directly from the physics of a flow problem. An accurate and unique determination of the boundary-vorticity values is essential. In the present approach, the boundary-vorticity values are determined from an integral constraint derived from the velocity-integral representation. The theoretical foundation of the boundary-vorticity evaluation was established by Wu (ref. 1).

Airfoils in the physical plane ( $z$ -plane) are conformally transformed into simple geometries in the computational plane ( $\zeta$ -plane). By using conformal mapping, the integral representation of the velocity vector, derived in the physical plane, can be directly used in the computational plane. The vorticity-transport equation is also in its simplest possible form in the computational plane. In addition, the circulation of a passing vortex is unchanged by the transformation between the two planes. A fast Fourier transform can be applied to the computational procedure, resulting in the present, efficient computer code ZETA II.

## Conformal Mapping of Two-Element Airfoils

The conformal mapping technique used in this study was introduced by Ives (ref. 2) and modified by Hall and Suddhoo (ref. 3). In particular, a slatted-airfoil geometry is transformed from the physical plane to two concentric circles in the transformed plane. The following mapping steps are involved in this transformation:

1. A Karman–Treffitz transformation maps the slat onto a near circle while the main airfoil deforms slightly.
2. Another Karman–Treffitz transformation maps the main airfoil configuration onto a near circle while the near circle corresponding to the slat deforms slightly.
3. A Theodorsen numerical transformation maps the near circle corresponding to the main airfoil onto a unit circle. The near circle corresponding to the slat deforms slightly again. The near circle is located outside the unit circle.
4. A bilinear transformation maps the near circle from outside the unit circle to a near circle inside the unit circle. The external-flow problem is now converted into an internal-flow problem. The far-field boundary of the external-flow problem is mapped onto a singular point located on the real axis in the annular region.
5. A Garrick–Theodorsen numerical transformation maps the near circle onto a circle. The singular point will, in general, move off the real axis.
6. A rotation brings the singular point back to the real axis in the transformed plane.

The above transformation steps can be used to transform any two-element airfoil geometry (e.g., an airfoil-flap configuration). For problems with a point vortex moving in the fluid, the location of the vortex at any instant can be easily correlated between the physical and the computational planes. In this case, the transformation procedure reduces to a simpler procedure that transforms a single airfoil onto a unit circle. This procedure allows an airfoil to perform different types of deformation and the shape to be transformed conformally. In the simpler procedure, only steps 2, 3, and 4 are needed, and the singular point is located at the origin of the computational plane.

## Kinematics

The integral representation of the velocity vector  $\vec{v}$  in the  $\zeta$ -plane (in cylindrical coordinates  $\rho, \phi$ ), with a passing-point vortex of circulation  $\vec{\Gamma}_P$  at a location  $\vec{\rho}_P$ , is:

$$\vec{v}(\vec{\rho}) = - \int_R \vec{\omega}_o H_o^2 \times \vec{Q} dR_o + \int_B [(\vec{v}_o \cdot \vec{n}_o) - (\vec{v}_o \times \vec{n}_o) \times] \vec{Q} dB_o + \left( \frac{1}{2\pi} \right) \left( \frac{\vec{\Gamma}_P \times (\vec{\rho} - \vec{\rho}_P)}{|\vec{\rho} - \vec{\rho}_P|^2} \right) \quad (1)$$

where  $\vec{\omega}$  is the vorticity vector;  $H$  is the scale factor of the transformation,  $H = |dz/d\zeta|$ ;  $B$  is the boundary of the fluid region  $R$ ;  $\vec{n}$  is a unit normal vector on  $B$  directed outward from  $R$ ; the subscript

$o$  indicates that a variable or an integration is in the  $\vec{\rho}_o$  space; and  $\vec{Q}$  is the gradient of the fundamental solution of elliptic equations

$$\vec{Q} = \frac{\vec{\rho}_o - \vec{\rho}}{2\pi|\vec{\rho}_o - \vec{\rho}|^2}$$

The boundary integral in equation (1) represents the velocity boundary contributions. It includes the solid-body motions and the free-stream velocity if the reference frame is moving with the solid bodies at a velocity  $-\vec{v}_\infty$ , where  $\vec{v}_\infty$  is the free-stream velocity. It may also include the surface velocity in the case where the body is undergoing a deforming motion.

In the transformed plane, the singular point introduced by the bilinear transformation represents the far-field boundary that is infinitely far from the solid bodies. The boundary  $B$  in equation (1), therefore, must include an infinitesimal circle surrounding the singular point. The boundary integral around this small circle can be analytically evaluated since the velocity on the circle is known through the conformal transformation. After the analytical integration on this circle, the singular point is mathematically excluded from the computational plane. In actual computations, a small but finite region around the singular point is removed. In the physical plane, the removal of this singular region represents the computation region in a finite region surrounding the solids. The excluded region, in general, contains vorticity. For example, for a steady flow around an airfoil at a small angle of attack, the excluded region contains the starting vortices that are shed from the vicinity of the airfoil. For a general, unsteady flow, the region contains no vorticity at the beginning but may contain vorticity later on as the vorticity that is shed by the airfoil eventually reaches this region. The excluded region, therefore, may possess a circulation. In the transformed plane, the singular region serves as a vortex sink, which draws the vorticity that was shed earlier from the vicinity of the solids. The circulation of the excluded region contributes to the velocity field in the transformed plane in accordance with the Biot–Savart law. Taking the above into consideration, one has from equation (1),

$$\vec{v} = - \int_R \vec{\omega}_o H_o^2 \times \vec{Q} dR_o + \vec{v}_S + \frac{\Gamma_S}{2\pi} \vec{v}_\Gamma + \int_{S_1+S_2} [(\vec{v}_o \cdot \vec{n}_o) - (\vec{v}_o \times \vec{n}_o) \times] \vec{Q} dB_o + \frac{\Gamma_P}{2\pi} \vec{v}_P \quad (2)$$

where the integrals over  $S_1$  and  $S_2$  represent the velocity contributions from the solid motion of the slat and the main elements of the airfoil, respectively (for the case of a slatted airfoil);  $\Gamma_S$  is the circulation of the excluded region;  $\vec{v}_\Gamma$  represents the contribution from  $\Gamma_S$  per unit circulation; and  $\vec{v}_S$  is the contribution from the free stream that has been integrated analytically. Considering the bilinear transformation,

$$z = \frac{1 - \bar{a}\zeta}{\zeta - \bar{a}} \quad (3)$$

that transforms the infinity boundary in the  $z$ -plane to a point located at  $\bar{a}$  on the real axis of the  $\zeta$ -plane, one has

$$\begin{aligned}
\vec{v}_S &= v_{S_\rho} \vec{e}_\rho + v_{S_\phi} \vec{e}_\phi \\
&= \frac{v_\infty(\bar{a} - 1)}{(\rho^2 + \bar{a}^2 - 2\bar{a}\rho \cos \phi)^2} \left\{ \left[ \cos \alpha_\infty ((\bar{a}^2 + \rho^2) \cos \phi - 2\bar{a}\rho) + \sin \alpha_\infty (\bar{a}^2 - \rho^2) \sin \phi \right] \vec{e}_\rho \right. \\
&\quad \left. + \left[ \sin \alpha_\infty ((\bar{a}^2 + \rho^2) \cos \phi - 2\bar{a}\rho) - \cos \alpha_\infty (\bar{a}^2 - \rho^2) \sin \phi \right] \vec{e}_\phi \right\} \quad (4)
\end{aligned}$$

where  $\vec{e}_\rho$  and  $\vec{e}_\phi$  denote the unit directional vectors in the  $\zeta$ -plane and  $\alpha_\infty$  is the angle of attack. In the present problem, the contribution from the singular point retains the same form of equation (4) since the bilinear transformation for the singular point basically has the same form. The contribution from the singular point also includes the effects of scale factors that appear in transformations other than the bilinear transformation.

The velocity vector  $\vec{v}_\Gamma$  in equation (2) is

$$\begin{aligned}
\vec{v}_\Gamma &= v_{\Gamma_\rho} \vec{e}_\rho + v_{\Gamma_\phi} \vec{e}_\phi \\
&= \frac{-\bar{a} \sin \phi}{\rho^2 + \bar{a}^2 - 2\bar{a}\rho \cos \phi} \vec{e}_\rho + \frac{\rho - \bar{a} \cos \phi}{\rho^2 + \bar{a}^2 - 2\bar{a}\rho \cos \phi} \vec{e}_\phi \quad (5)
\end{aligned}$$

## Fourier Series Expansion

Let the two components of the velocity vector be  $v_\rho$  and  $v_\phi$ . From equation (2), one has

$$\begin{aligned}
v_\rho &= \frac{1}{2\pi} \int_R \frac{\omega_o H_o^2 \rho_o \sin(\phi_o - \phi)}{\rho_o^2 + \rho^2 - 2\rho_o \rho \cos(\phi_o - \phi)} \rho_o d\rho_o d\phi_o + \frac{1}{2\pi} \int_{S_1+S_2} \frac{v_{\rho_o} [\rho_o \cos(\phi_o - \phi) - \rho]}{\rho_o^2 + \rho^2 - 2\rho_o \rho \cos(\phi_o - \phi)} \rho_o d\phi_o \\
&\quad - \frac{1}{2\pi} \int_{S_1+S_2} \frac{v_{\phi_o} \rho_o \sin(\phi_o - \phi)}{\rho_o^2 + \rho^2 - 2\rho_o \rho \cos(\phi_o - \phi)} \rho_o d\phi_o + v_{S_\rho} + \frac{\Gamma_S}{2\pi} v_{\Gamma_\rho} + \frac{\Gamma_P}{2\pi} v_{P_\rho} \quad (6)
\end{aligned}$$

$$\begin{aligned}
v_\phi &= - \frac{1}{2\pi} \int_R \frac{\omega_o H_o^2 [\rho_o \cos(\phi_o - \phi) - \rho]}{\rho_o^2 + \rho^2 - 2\rho_o \rho \cos(\phi_o - \phi)} \rho_o d\rho_o d\phi_o + \frac{1}{2\pi} \int_{S_1+S_2} \frac{v_{\rho_o} \rho_o \sin(\phi_o - \phi)}{\rho_o^2 + \rho^2 - 2\rho_o \rho \cos(\phi_o - \phi)} \rho_o d\phi_o \\
&\quad + \frac{1}{2\pi} \int_{S_1+S_2} \frac{v_{\phi_o} [\rho_o \cos(\phi_o - \phi) - \rho]}{\rho_o^2 + \rho^2 - 2\rho_o \rho \cos(\phi_o - \phi)} \rho_o d\phi_o + v_{S_\phi} + \frac{\Gamma_S}{2\pi} v_{\Gamma_\phi} + \frac{\Gamma_P}{2\pi} v_{P_\phi} \quad (7)
\end{aligned}$$

The velocity components and the vorticity are expanded in Fourier series as follows:

$$\begin{aligned}
v_\rho &= \frac{\bar{a}_0(\rho)}{2} + \sum_1^N [\bar{a}_n(\rho) \cos n\phi + \bar{b}_n(\rho) \sin n\phi] \\
v_\phi &= \frac{\bar{c}_0(\rho)}{2} + \sum_1^N [\bar{c}_n(\rho) \cos n\phi + \bar{d}_n(\rho) \sin n\phi] \\
\omega H^2 &= \frac{\bar{\alpha}_0(\rho)}{2} + \sum_1^N [\bar{\alpha}_n(\rho) \cos n\phi + \bar{\beta}_n(\rho) \sin n\phi] \\
v_{S_\rho} &= \frac{\bar{x}_0(\rho)}{2} + \sum_1^N [\bar{x}_n(\rho) \cos n\phi + \bar{y}_n(\rho) \sin n\phi] \\
v_{S_\phi} &= \frac{\bar{s}_0(\rho)}{2} + \sum_1^N [\bar{s}_n(\rho) \cos n\phi + \bar{t}_n(\rho) \sin n\phi] \\
v_{\Gamma_\rho} &= \frac{\bar{e}_0(\rho)}{2} + \sum_1^N [\bar{e}_n(\rho) \cos n\phi + \bar{f}_n(\rho) \sin n\phi] \\
v_{\Gamma_\phi} &= \frac{\bar{g}_0(\rho)}{2} + \sum_1^N [\bar{g}_n(\rho) \cos n\phi + \bar{h}_n(\rho) \sin n\phi] \\
v_{P_\rho} &= \frac{\bar{p}_0(\rho)}{2} + \sum_1^N [\bar{p}_n(\rho) \cos n\phi + \bar{q}_n(\rho) \sin n\phi] \\
v_{P_\phi} &= \frac{\bar{i}_0(\rho)}{2} + \sum_1^N [\bar{i}_n(\rho) \cos n\phi + \bar{j}_n(\rho) \sin n\phi]
\end{aligned} \tag{8}$$

Substituting equation (8) into equations (6) and (7) and then performing an analytical integration in the  $\phi$ -direction yields the following velocity Fourier coefficients:

$$\begin{aligned}
\bar{a}_0(\rho) &= \bar{a}_0(\rho_S) \left( \frac{\rho_S}{\rho} \right) + \bar{x}_0(\rho) + \bar{e}_0(\rho) \left( \frac{\Gamma_S}{2\pi} \right) + \bar{p}_0(\rho) \left( \frac{\Gamma_P}{2\pi} \right) \\
\bar{a}_n(\rho) &= \frac{1}{2} \int_{\rho_S}^{\rho} \bar{\beta}_n(\rho_o) \left( \frac{\rho_o}{\rho} \right)^{n+1} d\rho_o + \frac{1}{2} \int_{\rho}^1 \bar{\beta}_n(\rho_o) \left( \frac{\rho}{\rho_o} \right)^{n-1} d\rho_o \\
&\quad + \frac{1}{2} \bar{a}_n(1) \rho^{n-1} + \frac{1}{2} \bar{a}_n(\rho_S) \left( \frac{\rho_S}{\rho} \right)^{n+1} - \frac{1}{2} \bar{d}_n(1) \rho^{n-1} \\
&\quad + \frac{1}{2} \bar{d}_n(\rho_S) \left( \frac{\rho_S}{\rho} \right)^{n+1} + \bar{x}_n(\rho) + \bar{e}_n(\rho) \left( \frac{\Gamma_S}{2\pi} \right) + \bar{p}_n(\rho) \left( \frac{\Gamma_P}{2\pi} \right) \\
\bar{b}_n(\rho) &= - \frac{1}{2} \int_{\rho_S}^{\rho} \bar{\alpha}_n(\rho_o) \left( \frac{\rho_o}{\rho} \right)^{n+1} d\rho_o - \frac{1}{2} \int_{\rho}^1 \bar{\alpha}_n(\rho_o) \left( \frac{\rho}{\rho_o} \right)^{n-1} d\rho_o \\
&\quad + \frac{1}{2} \bar{b}_n(1) \rho^{n-1} + \frac{1}{2} \bar{b}_n(\rho_S) \left( \frac{\rho_S}{\rho} \right)^{n+1} + \frac{1}{2} \bar{c}_n(1) \rho^{n-1} \\
&\quad - \frac{1}{2} \bar{c}_n(\rho_S) \left( \frac{\rho_S}{\rho} \right)^{n+1} + \bar{y}_n(\rho) + \bar{f}_n(\rho) \left( \frac{\Gamma_S}{2\pi} \right) + \bar{q}_n(\rho) \left( \frac{\Gamma_P}{2\pi} \right) \\
\bar{c}_0(\rho) &= \int_{\rho_S}^{\rho} \bar{\alpha}_0(\rho_o) \frac{\rho_o}{\rho} d\rho_o + \bar{c}_0(\rho_S) \left( \frac{\rho_S}{\rho} \right) + \bar{s}_0(\rho) + \bar{g}_0(\rho) \left( \frac{\Gamma_S}{2\pi} \right) + \bar{i}_0(\rho) \left( \frac{\Gamma_P}{2\pi} \right) \\
\bar{c}_n(\rho) &= \frac{1}{2} \int_{\rho_S}^{\rho} \bar{\alpha}_n(\rho_o) \left( \frac{\rho_o}{\rho} \right)^{n+1} d\rho_o - \frac{1}{2} \int_{\rho}^1 \bar{\alpha}_n(\rho_o) \left( \frac{\rho}{\rho_o} \right)^{n-1} d\rho_o \\
&\quad + \frac{1}{2} \bar{b}_n(1) \rho^{n-1} - \frac{1}{2} \bar{b}_n(\rho_S) \left( \frac{\rho_S}{\rho} \right)^{n+1} + \frac{1}{2} \bar{c}_n(1) \rho^{n-1} \\
&\quad + \frac{1}{2} \bar{c}_n(\rho_S) \left( \frac{\rho_S}{\rho} \right)^{n+1} + \bar{s}_n(\rho) + \bar{g}_n(\rho) \left( \frac{\Gamma_S}{2\pi} \right) + \bar{i}_n(\rho) \left( \frac{\Gamma_P}{2\pi} \right) \\
\bar{d}_n(\rho) &= \frac{1}{2} \int_{\rho_S}^{\rho} \bar{\beta}_n(\rho_o) \left( \frac{\rho_o}{\rho} \right)^{n+1} d\rho_o - \frac{1}{2} \int_{\rho}^1 \bar{\beta}_n(\rho_o) \left( \frac{\rho}{\rho_o} \right)^{n-1} d\rho_o \\
&\quad - \frac{1}{2} \bar{a}_n(1) \rho^{n-1} + \frac{1}{2} \bar{a}_n(\rho_S) \left( \frac{\rho_S}{\rho} \right)^{n+1} + \frac{1}{2} \bar{d}_n(1) \rho^{n-1} \\
&\quad + \frac{1}{2} \bar{d}_n(\rho_S) \left( \frac{\rho_S}{\rho} \right)^{n+1} + \bar{t}_n(\rho) + \bar{h}_n(\rho) \left( \frac{\Gamma_S}{2\pi} \right) + \bar{j}_n(\rho) \left( \frac{\Gamma_P}{2\pi} \right)
\end{aligned} \tag{9}$$

In equation (9),  $1 \leq n \leq N$  and  $a_0(\rho_S)$ ,  $a_n(\rho_S)$ ,  $b_n(\rho_S)$  ... etc. represent the Fourier coefficients of the velocity boundary conditions at  $\rho = \rho_S$ . The small circle of radius  $\rho_S$  corresponds to the slat in the physical plane. The velocity Fourier coefficients,  $a_0(1)$ ,  $a_n(1)$ ,  $b_n(1)$  ... etc., are the velocity boundary conditions at  $\rho = 1$ , which denotes the main airfoil. For a single-airfoil case, equation (9) is simplified by dropping the terms containing  $\rho_S$ .

The usage of the Fourier series offers important advantages in the numerical process. It not only increases the solution accuracy, but it also drastically reduces the computational work. Each velocity Fourier coefficient relates to the corresponding vorticity Fourier coefficient by a simple, one-dimensional

integral. Also, the integral relations stated in equation (9) give explicitly a series of constraint equations on the vorticity Fourier coefficients that allows the explicit evaluation of the vorticity values on the solid surfaces.

## Vorticity Integral Constraints

The vorticity values on the solid surfaces are determined by satisfying the velocity boundary conditions. If one applies equation (2) on the solid surfaces  $S_1$  and  $S_2$ , the constraint equations for the vorticity field result because the velocity on the surface is given and the velocities induced by  $\Gamma_S$  and  $\Gamma_P$  are known. The vorticity field, therefore, is restricted by the domain integral. Using the Fourier series with equation (9) yields the constraint equations for the vorticity Fourier coefficients when  $\rho = \rho_S$ :

$$\begin{aligned} \int_{\rho_S}^1 \bar{\alpha}_n(\rho_o) \left( \frac{\rho_S}{\rho_o} \right)^{n-1} d\rho_o &= \bar{b}_n(1) \rho_S^{n-1} - \bar{b}_n(\rho_S) + \bar{c}_n(1) \rho_S^{n-1} - \bar{c}_n(\rho_S) \\ &\quad + 2\bar{s}_n(\rho_S) + \bar{g}_n(\rho_S) \left( \frac{\Gamma_S}{\pi} \right) + \bar{q}_n(\rho_S) \left( \frac{\Gamma_P}{\pi} \right) \\ \int_{\rho_S}^1 \bar{\beta}_n(\rho_o) \left( \frac{\rho_S}{\rho_o} \right)^{n-1} d\rho_o &= -\bar{a}_n(1) \rho_S^{n-1} + \bar{a}_n(\rho_S) + \bar{d}_n(1) \rho_S^{n-1} - \bar{d}_n(\rho_S) \\ &\quad + 2\bar{t}_n(\rho_S) + \bar{h}_n(\rho_S) \left( \frac{\Gamma_S}{\pi} \right) + \bar{j}_n(\rho_S) \left( \frac{\Gamma_P}{\pi} \right) \end{aligned} \quad (10)$$

At  $\rho = 1$ ,

$$\begin{aligned} \int_{\rho_S}^1 \bar{\alpha}_n(\rho_o) \rho_o^{n+1} d\rho_o &= \bar{c}_n(1) - \bar{c}_n(\rho_S) \rho_S^{n+1} - \bar{b}_n(1) + \bar{b}_n(\rho_S) \rho_S^{n+1} \\ &\quad - 2\bar{s}_n(1) - \bar{g}_n(1) \left( \frac{\Gamma_S}{\pi} \right) - \bar{q}_n(1) \left( \frac{\Gamma_P}{\pi} \right) \\ \int_{\rho_S}^1 \bar{\beta}_n(\rho_o) \rho_o^{n+1} d\rho_o &= \bar{d}_n(1) - \bar{d}_n(\rho_S) \rho_S^{n+1} + \bar{a}_n(1) - \bar{a}_n(\rho_S) \rho_S^{n+1} \\ &\quad - 2\bar{t}_n(1) - \bar{h}_n(1) \left( \frac{\Gamma_S}{\pi} \right) - \bar{j}_n(1) \left( \frac{\Gamma_P}{\pi} \right) \end{aligned} \quad (11)$$

Once the values for  $\bar{\alpha}_n$  and  $\bar{\beta}_n$  in the interior of the flow domain are known, equations (10) and (11) give a unique determination of  $\bar{\alpha}_n$  and  $\bar{\beta}_n$ , where  $1 \leq n \leq N$  at both  $\rho = \rho_S$  and  $\rho = 1$ . Notice that these integral constraints are obtained by satisfying the boundary condition on either  $v_\phi$ , the tangential velocity component, or  $v_\rho$ , the normal velocity component, on the solid surfaces.

To determine  $\bar{\alpha}_0$  at  $\rho = \rho_S$  and at  $\rho = 1$ , however, one needs additional information. If the individual circulations around the two closed paths that enclose the slatted and the main airfoils in the  $\zeta$ -plane are known, one has

$$\begin{aligned}\int_{R_1} \omega H^2 dR &= \Gamma_1 \\ \int_{R_2} \omega H^2 dR &= \Gamma_2\end{aligned}\tag{12}$$

where  $R_1$  and  $R_2$  denote the flow domains enclosed by the two paths around the slatted and the main airfoils, respectively. The circulations  $\Gamma_1$  and  $\Gamma_2$  are known by tracking the vorticity flowing out of  $R_1$  and  $R_2$  at every time step. The principle of conservation of total vorticity gives

$$\Gamma_1 + \Gamma_2 = -\Gamma_3\tag{13}$$

where  $\Gamma_3$  includes the integrated value of  $\omega H^2$  in the remaining computational domain and  $\Gamma_S$ . Using equation (8) on the Fourier series expansion of  $\omega H^2$ , one gets the constraints for  $\alpha_0$  from equation (12):

$$\begin{aligned}\int_{\rho_S}^{\rho_1} \bar{\alpha}_0(\rho_o) \rho_o d\rho_o &= \frac{\Gamma_1}{\pi} \\ \int_{\rho_2}^1 \bar{\alpha}_0(\rho_o) \rho_o d\rho_o &= \frac{\Gamma_2}{\pi}\end{aligned}\tag{14}$$

where  $\rho_1$  and  $\rho_2$  represent the radii of the two individual closed paths in the  $\zeta$ -plane.

## Kinetics

The kinetic aspect of the flow problem is described by the vorticity-transport equation. In the computational plane, the equation is

$$H^2 \frac{\partial \vec{\omega}}{\partial t} = \nabla \times (\vec{v} - \vec{v}_G) \times \vec{\omega} + \nabla \cdot (\nu \nabla \vec{\omega})\tag{15}$$

where  $t$  denotes the time and  $\nu$  represents the kinematic viscosity of the fluid. For turbulent-flow calculations,  $\nu$  includes an eddy viscosity that is computed here by the Baldwin and Lomax algebraic model (ref. 4). The velocity  $\vec{v}_G$  represents the grid velocity observed in the computational plane during the airfoil deformation. In the attached-flow zones, the last term of equation (15) is simplified to  $\partial/\partial n(\nu \partial \omega / \partial n)$ , where  $n$  is the normal coordinate perpendicular to the streamwise direction. The vorticity-transport equation becomes a parabolic type in the attached-flow zones. For problems containing a passing-point vortex, the vortex travels in the flow field with a local velocity that is induced by all the distributed vorticity existing in the flow field and also by the circulation  $\Gamma_S$ . The circulation carried by the point vortex  $\Gamma_P$  is unchanged during its motion in the fluid.

One of the advantages of using the vorticity-transport equation is that the pressure is eliminated from the mathematical formulation. The pressure on the solid surfaces, wherever needed, is usually

obtained from the normal gradient of the computed vorticity on the surface (ref. 5). Hence, with this approach, an accurate determination of the normal gradient of the vorticity field is required. However, this task is difficult when both the magnitude and the gradient of the boundary-vorticity values are large, as they usually are in high-Reynolds-number flows. In particular, for turbulent-flow computations, the modeling of flow turbulence usually requires the assumption that different sublayers exist near the solid surfaces. Substantial uncertainties and inaccuracies in the vorticity-normal gradient are implicit in such models. To eliminate these difficulties, the present authors reformulated the pressure as an integral representation by using a principal solution of the Poisson equation (ref. 6). Since the Poisson equation is the principal solution of the kinematics, that is, the instantaneous relationship between the velocity and vorticity fields, it is independent of time. It is demonstrated in reference 6 that this formulation yields accurate pressure solutions. In the present study, this formulation is extended to include multielement airfoils. The pressure can be computed from the following integral expression:

$$h(\vec{\rho}) - \int_S h_0 \vec{Q} \cdot \vec{n}_0 dB_0 = \frac{p_\infty}{\delta_\infty} + \int_R (\vec{v}_0 \times \vec{\omega}_0) \cdot \vec{Q} dR_0 + \nu \int_S (\vec{\omega}_0 \times \vec{Q}) \cdot \vec{n}_0 dB_0 \\ - \int_S \left( \frac{1}{2\pi} \ln \frac{1}{|\vec{\rho}_o - \vec{\rho}|} \right) \frac{\partial \vec{v}_0}{\partial t} \cdot \vec{n}_0 dB_0$$

where  $h$  is the total head, and it is computed by the Fredholm integral equation of the second kind.

## NUMERICAL FORMULATIONS

In the present computation, the airfoil is first transformed to a simple geometry in the computational plane, and then the computations are performed in this plane. The computational grid is generated by the numerical, conformal mapping, with proper control on both the radial and the circumferential directions in the computational plane. If the airfoil undergoes a time-dependent deformation, the conformal mapping is performed at every time step. The following steps constitute a complete computation cycle, which advances the velocity and the vorticity solutions from an old time level to a new time level:

1. Perform the numerical, conformal mapping when the airfoil deforms. The grid velocity,  $\vec{v}_G$ , is numerically evaluated in the physical plane and then transformed to the computational plane.
2. Compute the convection velocity of the point vortex in the computational plane,  $\vec{v}_P$ . This velocity is that which is induced by all the distributed vorticity existing in the flow field and also by  $\Gamma_S$ . The distance traveled by the point vortex during a time step,  $\Delta t$ , is  $\vec{v}_P \Delta t / H^2$  (where  $H^2$  is the Jacobian).
3. Compute the distributed vorticity (excluding the surface vorticity, which will be computed in step 4) for the new time level by solving the vorticity-transport equation (15).
4. Determine the surface vorticity, where the new distributed vorticity is obtained from step 3 and the new location of the point vortex is known from step 2.
5. Compute the velocity in the vortical region for the new time level by using equation (9).

In step 3, the vorticity values in the detached-flow zones are obtained by solving a fully implicit finite-difference equation discretized from the vorticity-transport equation. The time derivative is approximated by a one-step, forward-difference scheme, and the diffusion terms are approximated by central difference. The convection terms are approximated by a second-order, upwind-difference scheme (ref. 5). In the present procedure, a line-relaxation technique is used to solve the simultaneous, implicit, finite-difference equations. The line-relaxation technique involves an inversion of a tridiagonal matrix, where the unknown vorticity values on the same radial line are to be solved. The vorticity values on the adjacent radial lines are treated as known values; they are delayed by one iteration count in the relaxation procedure. During the iteration process, an under-relaxation factor is necessary.

The vorticity values in the attached-flow zones are computed by a marching procedure. The boundaries between the detached- and the attached-flow zones define the demarkation lines for the next time step. The vorticity values on the demarkation lines provide the initial condition for the vorticity in the attached zones, and they are part of the boundary conditions for the detached zones.

In step 4, the boundary-vorticity values adjacent to the solid surfaces are obtained through the integral constraint of the vorticity-Fourier coefficients. The converged interior-vorticity values obtained in step 3 are first transformed to the Fourier coefficients, in accordance with the  $\omega H^2$  expression in equation (8), along the circumferential direction at each constant radial station. For example,

$$\bar{\alpha}_n = \frac{1}{\pi} \int_0^{2\pi} \omega H^2 \cos(n\phi) d\phi \quad (16)$$

The integral in equation (16) is replaced by a numerical quadrature. Each vorticity-Fourier coefficient, except the constant coefficient, is subjected to the two associated integral-constraint equations (10) and (11). This allows the two values of the Fourier coefficient at  $\rho = \rho_S$  and at  $\rho = 1$  to be determined uniquely. The constant Fourier coefficient,  $\alpha_0$ , as stated earlier, is determined by the conservation of vorticity; that is, once the quantities of  $\Gamma_1$  and  $\Gamma_2$  in equation (12) are known, the boundary values of this Fourier coefficient are determined by the two separated expressions in the equation. In the present, unsteady approach, the quantities  $\Gamma_1$  and  $\Gamma_2$  are tracked at each time level by recording the amount of vorticity flowing out of the regions  $R_1$  and  $R_2$ , respectively. After the Fourier coefficients at the boundaries are known, the vorticity at the boundaries can be easily determined from the  $\omega H^2$  expression in equation (8).

Steps 3 and 4 are repeated several times before the numerical procedure progresses to step 5. The updated boundary-vorticity values may not equal the boundary values used in step 3 to compute the interior-vorticity values. Once the maximum difference between the updated boundary-vorticity values and the previous boundary values is less than a prescribed criterion, the computation then is advanced to step 5. In order to make the process convergent, an under-relaxation factor on the boundary-vorticity values is necessary. In step 5 the interior-velocity Fourier coefficients are calculated by numerical quadrature of the vorticity Fourier coefficients, equation (9). That is, only one-dimensional quadrature is involved for each of the velocity Fourier coefficients. The velocity values are then obtained from the  $v_\rho$  and  $v_\phi$  expressions in equation (8).

The numerical, conformal mapping procedures are coded in a separate computation module. This module is executed only once when the airfoil does not deform, but it is executed at every time step if the airfoil undergoes a time-dependent deformation. The main module of the ZETA II code contains the numerical procedures as described by steps 1 to 5. The surface pressure is computed by another module that acquires the velocity and vorticity that are computed by the main module. The module that computes the surface pressure also computes the skin friction and the aerodynamic loads.

The ZETA II code is used to demonstrate new concepts that are useful in improving the rotor aerodynamic characteristics. The present effort is focused on problems of dynamic stall and BVI noise. The benefits from several new concepts are demonstrated by comparing the numerical results for the basic, single-element airfoil with those obtained for the slatted airfoil and the deformable airfoil.

## DYNAMIC STALL

Several concepts have been pursued by U.S. Army researchers at AFDD in order to decrease and even to eliminate the undesirable occurrence of dynamic stall. These concepts can be categorized as either active or passive devices. The active devices include airfoils with blowing/suction on the leeward side and airfoils with different types of deformation; the passive devices include airfoils with an added slat or slot geometry. In the present study, the slatted airfoil and several types of deformable airfoils are investigated. These various configurations are based on the Boeing-Vertol VR-7 airfoil.

### Slatted Airfoils

Flow solutions around the basic, single-element VR-7 airfoil and the slatted VR-7 airfoil were obtained by using the ZETA II code. The Reynolds number ( $Re$ ), based on the airfoil chord, is 200,000. A steady flow is fully established around the airfoil at a small angle of attack before the airfoil undergoes oscillating motion. The reduced frequency ( $k$ ), normalized by the airfoil half chord and the oscillating frequency, is 0.1 in the results reported herein.

The grids used to predict the load characteristics are  $81 \times 51$  and  $121 \times 61$  divisions for the basic and the slatted airfoils, respectively. Figure 1 shows sample grids around the basic and the slatted airfoils. Closeup views of the grids and the slat geometries are also shown in the figure. The pitching axis for both the basic and the slatted VR-7 airfoils passes through the quarter-chord location of the main airfoil, and the airfoil oscillates sinusoidally from  $5^\circ$  to  $25^\circ$ . The experimental hysteresis loops for the lift, drag, and pitching-moment coefficients are shown in figure 2; measurements were made by AFDD researchers in their water tunnel. The dynamic stall of the basic VR-7 airfoil (solid line) is quite evident. The lift-coefficient curve increases for angles of attack up to about  $19^\circ$  and then it maintains a constant value for about  $1^\circ$ . Then the lift coefficient increases again because of the formation of a leading-edge stall vortex. The airfoil experiences a large nosedown pitching moment as the vortex moves over the upper surface. When the vortex leaves the airfoil, the lift drops drastically. As for the slatted VR-7 airfoil (dashed line), no stall vortex forms around the leading edge. The pitching moment shows no sign of a rapid change at higher angles of attack, and no abrupt drop in the lift occurs.

The numerical calculation is initiated with the airfoil at  $\alpha = 5^\circ$  and the flow impulsively started from rest. Once the solution converges, the oscillating motion of the airfoil is allowed to begin. The predicted lift, drag, and moment hysteresis data for the basic airfoil are shown in figure 3. The shape of each loop compares well with the test data, but the predicted lift loop is consistently lower than the test results. The computed streamline patterns at selected angles of attack are shown in figure 4. The lift and pitching-moment loops are shown again in this figure to demonstrate the flow features in connection with the dynamic stall. The formation of a leading-edge stall vortex and its movement from  $\alpha = 22.93^\circ$  to  $\alpha = 24.34^\circ$  correspond to the rise in lift and the large change in pitching moment. When the stall vortex leaves the airfoil, the lift drops sharply. The flow remains separated during the downstroke portion of the cycle until  $\alpha \approx 12^\circ$ , but the lift and the pitching moment are maintained approximately at the same level throughout the downstroke period. The instantaneous streamlines and the surface pressure for the slatted airfoil are shown in figure 5; dotted lines in the  $C_p$  plots represent the slatted airfoil, and solid lines represent the main airfoil. The shapes of the hysteresis loops are quite similar to those of the test results in figure 2. The slatted airfoil does not show the formation of the leading-edge vortex. The flow around the leading edge of the main airfoil remains attached during the complete cycle. The flow starts to separate from the trailing edge of the airfoil at about  $\alpha = 15^\circ$ , and the separated flow never propagates to the leading edge.

## Deformable Airfoils

Three types of airfoil deformation are considered in the present study: (1) nose deflection; (2) camber; and (3) thickness. A representative of each type of deformed airfoil is shown in figure 6. During the oscillation motion, the airfoil deforms sinusoidally in proportion to the angle of attack; that is, the airfoil has no deformation at the beginning of the oscillation and has maximum deformation at the maximum angle of attack. The computed cases are for flows at a reduced frequency of 0.15 and a Reynolds number of one million. The flow is assumed to be fully turbulent.

Figure 7 shows the surface pressures and instantaneous streamlines at selected angles of attack during the oscillation cycle of the basic airfoil. The separation streamline starts from the trailing edge of the airfoil and moves upstream as the angle of attack increases. At  $\alpha = 25^\circ$ , the separation line almost reaches the leading edge of the airfoil. A leading-edge vortex is present at this angle of attack, but the load-hysteresis loops that are shown in figure 8 indicate that the lift drop for the airfoil begins at a much lower angle (at approximately  $21.5^\circ$ ). The initial lift drop is caused by the spreading of the separation bubble that is present over the trailing edge of the airfoil. The sharp lift increase that follows the initial lift drop is caused by the rapid formation and growth of the leading-edge vortex. The vortex then appears to merge with the trailing-edge separation bubble, causing an abrupt second-phase lift drop, which corresponds to the lift stall. The airfoil experiences a large nosedown pitching moment near the maximum angle of attack. The difference between the load-hysteresis loops shown in figure 8 and those shown in figure 3 is mainly due to the difference in the reduced frequency.

The instantaneous streamlines and surface pressures for the nose-deflected airfoil are shown in figure 9. In this figure, the front 37.5 percent of the airfoil rotates down as the angle of attack increases. The maximum deflection angle is  $10^\circ$ . No leading-edge vortex is present for the case shown here. In figure 10, this case is represented by  $(0.375 c, 10^\circ)$ , where the first number denotes the portion of the airfoil that droops down and the second number denotes the maximum deflection angle. Three cases

were computed in the present study: (0.25 c, 10°), (0.375 c, 10°), and (0.50 c, 10°). Data for all three cases show that the leading-edge vortex is suppressed, and, therefore, no deep-lift stall is observed. The load-hysteresis loops shown in figure 10 suggest that, among the three cases computed, the (0.375 c, 10°) case has the best dynamic characteristics (note especially the improvement in the peak drag and pitching moment).

The next deformation studied was for an airfoil that changes camber as the angle of attack changes. The airfoil attains a maximum change in camber at the maximum angle of attack during the oscillation cycle. The maximum camber change studied herein is 5 percent of the airfoil chord. Three cases having different camber locations were computed: 40, 50, and 60 percent of the chord. The instantaneous streamlines and the surface pressures are shown in figure 11 for the case in which the camber is located at the 50-percent-chord location. The flow is similar to that of the previous nose-deflection case, but the surface pressure is smoother for the cambered case. The load-hysteresis loops for the three cambered cases are shown in figure 12. It can be seen that the 40- and 50-percent cases show similar dynamic characteristics, but the 50-percent case generates higher lift. Lift stall occurs for the 60-percent case, although it is much milder than that for the basic airfoil. The pitching-moment behavior is similar to that of the lift. The instantaneous streamlines for the 60-percent case, not shown here, indicate that the separation streamline has nearly reached the leading edge of the airfoil. The 50-percent case offers the best results among the cambered cases studied here.

The third airfoil deformation involves a thickness change. The airfoil thickens in proportion to its original thickness distribution, and the thickness reaches its maximum value at the maximum angle of attack during the airfoil oscillation. Three different thickness changes are studied: 25-, 50-, and 75-percent increases over the original thickness. Figure 13 shows the instantaneous streamlines and the surface pressures for the 50-percent-thickened case. As in the nose-deflection case, airfoil thickening also suppresses the formation of the leading-edge vortex. The load-hysteresis loops for the three computed cases, shown in figure 14, show that the lift stall is very mild for the 25-percent-thickened airfoil and is even milder for the other two airfoils. None of the airfoils experience moment stall. The 50-percent-thickened airfoil has the best dynamic characteristics among the three airfoils studied.

A comparison of the three types of airfoil deformation and the effect on the dynamic stall is seen in figure 15. Also shown are the loads for the basic airfoil. Clearly all three types have very similar drag characteristics and all three types eliminate the moment and lift stalls. The best pitching moment results from the thickening effect, whereas the best lift results from the cambering effect. It is concluded, however, that the best overall dynamic characteristics (among the three types of airfoil deformation that were studied) are achieved by varying the airfoil camber.

## VORTEX-AIRFOIL INTERACTIONS

Figure 16, a schematic of the vortex-airfoil interaction, shows a point vortex of clockwise sense passing under the airfoil. The flow around a Boeing VR-12 airfoil is computed for a fixed angle of attack of 5° and a Reynolds number of two million. Before introducing a point vortex into the flow field, a converged solution for an impulsively started airfoil is obtained. A point vortex of strength  $-0.2v_\infty c$ , where  $c$  is the airfoil chord length, is introduced at 5 chords upstream and 0.2 chord under

the airfoil camber line. The vortex causes the surface pressure to fluctuate and the boundary layer to thicken. In figure 17, the vorticity contours show a thickening of the boundary layer for two locations of the passing vortex. The  $X$ -location of the passing vortex,  $X_P$  in the figure, is referenced to the leading edge of the airfoil, and is normalized with the airfoil chord. In figure 18, the streamlines as well as the surface pressures are shown for different locations of the passing vortex. The effect of the passing vortex on the surface pressure appears clearly as a local suction perturbation on the lower surface where the pressure first decreases and then recovers. The pressure rise in the recovery region causes the boundary layer to thicken.

Figure 19 shows the variation of the pressure coefficient with respect to the location of the point vortex at selected points on the airfoil surface. Also shown in the figure is the pressure difference between the lower and upper surfaces at the same selected surface points. The large, unsteady variations in the surface pressure are the main cause of BVI noise. Comparing the amplitudes of the variations shows that the region close to the leading edge is a dominant source of BVI noise. For the cases studied, the passing vortex causes a temporary thickening of the boundary layer. A potential flow solution is clearly invalid in cases in which the strength of the vortex is sufficient to cause the boundary layer to separate. If the flow does not separate, then the pressure response predicted by the potential solution should match, at least to the first order, the pressure response obtained from the Navier-Stokes solution.

The feasibility of reducing the BVI noise by an active airfoil deformation was investigated. If the sense of the point vortex is such that the approaching vortex initially induces a downwash on the airfoil, the effective angle of attack will be temporarily reduced. To compensate for the resulting reduction in leading-edge suction, the front part of the airfoil is rotated upward as the point vortex approaches the airfoil. It then is rotated back as the vortex passes under the leading edge of the airfoil. Computations are presently limited to three locations for the center of rotation: 12.5, 25, and 37.5 percent of the airfoil chord, and two rotation angles:  $5^\circ$  and  $10^\circ$ , measured from the airfoil camber line. The effect of the airfoil deformation is demonstrated in figure 20, where the streamlines and the surface pressures are shown. In this figure, the case with the rotation centered at 25-percent chord and a rotation angle of  $5^\circ$  is shown ( $0.25 c, 5^\circ$ ). The front part of the airfoil starts to rotate upward at  $X_P = -0.26$ , reaches its maximum deflection angle at  $X_P = 0.02$ , and finally returns to its original position at  $X_P = 0.29$ .

In figure 21, the surface pressure at 5-percent chord is shown with respect to the  $X$ -location of the passing vortex. Also shown are the pressures for the basic airfoil and for another deformed case ( $0.25 c, 10^\circ$ ). Both of the deformed cases show an improvement in the unsteady pressure fluctuation on the lower surface; that is, not only is the amplitude of the pressure fluctuation reduced, but the slope of the pressure rise after the point vortex has passed the leading edge also is reduced. The amplitude of the pressure fluctuation is measured by the difference between the minimum pressure and the local maximum immediately after the point vortex passes the leading edge. The two deformed cases show a reduction in the magnitude of the fluctuation by approximately the same amount, about 30 percent of the original value. However, the ( $0.25 c, 10^\circ$ ) case results in a pressure that rises (or recovers) at a slower rate. This indicates that the  $10^\circ$  angle is a better choice for reducing the BVI noise that originates from the lower surface of the airfoil. On the upper surface, the pressure fluctuation is aggravated by the airfoil deformation. The amplitude of the pressure fluctuation is increased by 6 percent of the original value for the ( $0.25 c, 5^\circ$ ) case and by 15 percent for the ( $0.25 c, 10^\circ$ ) case. Here the magnitude of the pressure fluctuation is measured by the difference between the maximum pressure and the local minimum immediately after the point vortex passes the leading edge of the airfoil.

The overall improvement achieved in these two cases can be judged by comparing the resulting lift variation with that of the basic airfoil, as shown in figure 22. The figure shows that the (0.25 c, 5°) case is a better choice than the (0.25 c, 10°) case because the magnitude of the lift variation is smaller and the slope of the lift variation is milder. Similar results were obtained when comparisons were made between (0.125 c, 5°) and (0.125 c, 10°) and between (0.375 c, 5°) and (0.375 c, 10°).

Figure 23 shows a comparison of the computed pressures for the deformed cases (0.125 c, 5°), (0.25 c, 5°), and (0.375 c, 5°) with that of the basic airfoil. At the 5-percent-chord location, the pressure variation is most improved in the (0.375 c, 5°) case, even though this case is not much different from the (0.25 c, 5°) case. However, the pressure on the upper surface in the (0.375 c, 5°) case shows a clear advantage over the other two deformed cases. The unsteady lift is shown in figure 24, where it is evident that, among the present cases studied, the (0.375 c, 5°) case is the best for improving the unsteady-lift variation caused by the passing vortex. The drag and the moment coefficients are also shown in the figure. It should be noted that the reduction of the pressure fluctuation is accompanied by a drag rise and a larger fluctuation of the pitching moment.

## CONCLUSIONS

1. A numerical method, based on a vorticity-velocity formulation and an integral representation for the velocity vector, is extended for treating problems of multielement airfoils, deformable airfoils, and vortex-airfoil interactions. The high efficiency of the numerical approach offers an effective way of conducting parametric studies for the demonstration of new concepts. These concepts are applied to the design of helicopter blades in order to reduce dynamic stall and BVI noise. Under the present effort, a passive, slatted airfoil and an active, deformable airfoil were extensively investigated.
2. The dynamic stall can be reduced by adding a slat or by using airfoil deformation. Three types of airfoil deformation were investigated: airfoil nose deflection, airfoil camber change, and airfoil thickening. Even though all three are effective in reducing the dynamic stall, the most effective was found to be the camber change.
3. The BVI noise can be reduced by airfoil deformation. A particular type that was studied is the upward deflection of the front part of the airfoil as a vortex passes underneath it and close to the leading edge. The amplitude as well as the rate of variation of the pressure fluctuation on the lower surface of the airfoil are reduced. A best-deformation case was identified under the range of parameters studied in the present work.
4. The current ZETA II code is capable of predicting complex, unsteady flows under certain flow conditions. For laminar flows and high-Reynolds-number flows, the code predicts quantitatively well the aerodynamic loads and flow features. For flows of intermediate Reynolds numbers, where the laminar-turbulent transition is important, the code predicts well only qualitatively. The simple, eddy-turbulence model used here may not be adequate to treat this type of flow. Further investigations utilizing more accurate turbulence models are needed.
5. Other new concepts that are potentially capable of reducing dynamic stall and BVI noise can be investigated by the present ZETA II code with minor extensions or modifications. The surface blowing/suction case, for example, can be studied by modifying the velocity boundary condition in the

numerical procedure. The predicted aerodynamic characteristics with respect to a variety of parameters selected in the computation can provide a valuable guide for specifying a limited parameter set for experiments. The experiments also can determine the validity of the computer code.

## REFERENCES

1. Wu, J. C.: Numerical Boundary Conditions for Viscous Flow Problems. AIAA J., vol. 14, no. 8, 1976, pp. 1042-1049.
2. Ives, D. C.: A Modern Look at Conformal Mapping Including Multi-Connected Regions. AIAA J., vol. 14, no. 8, 1976, pp. 1006-1011.
3. Hall, I. M.; and Suddhoo, A.: Inviscid Compressible Flow Past a Multi-Element Airfoil. AGARD-CP-365, 1984.
4. Baldwin, Barrett S.; and Lomax, H.: Thin Layer Approximation and Algebraic Model for Separated Turbulent Flows. AIAA Paper 78-257, 1978.
5. Roache, Patrick J.: Computational Fluid Dynamics. Hermosa Publishers, Albuquerque, New Mexico, 1982.
6. Wang, C. M.; Wu, J. C.; and Tuncer, I. H.: Accurate Determination of Surface Pressure in High Reynolds Number Flows. Proceedings of the First International Conference on Computational Methods in Flow Analysis, Okayama, Japan, Sept. 1988.

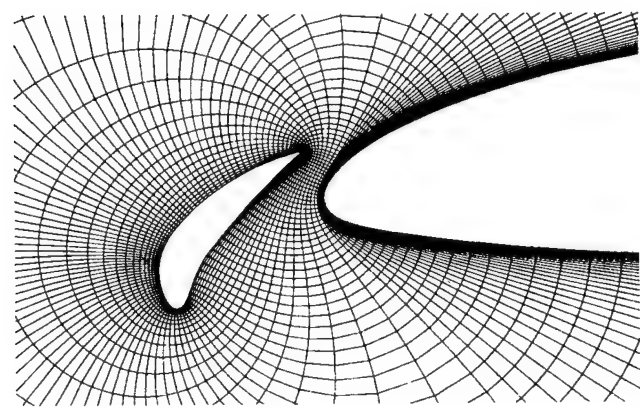
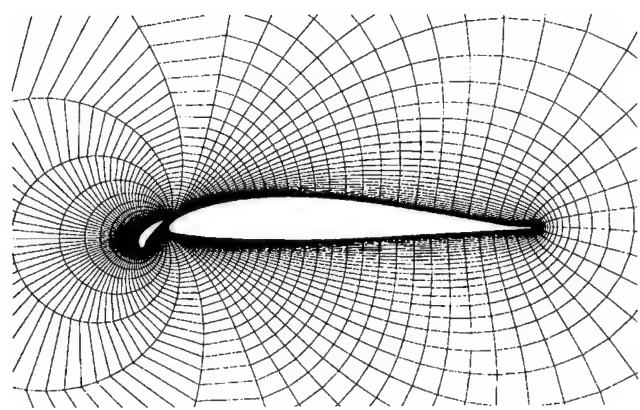
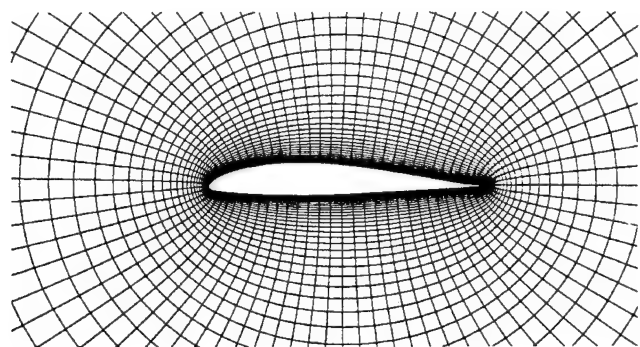


Figure 1. Grids of basic and slatted Boeing-Vertol VR-7 airfoils.

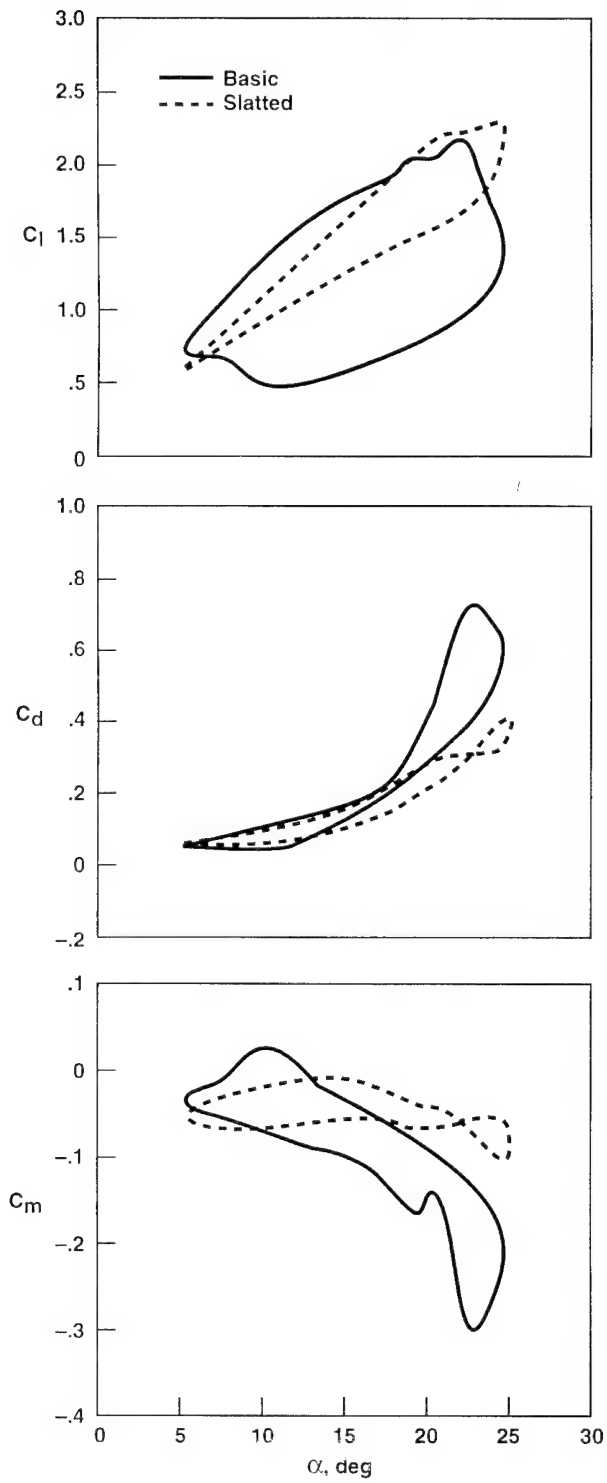


Figure 2. Experimental load-hysteresis loop for the VR-7 airfoil at  $Re = 200,000$  and  $k = 0.1$ .

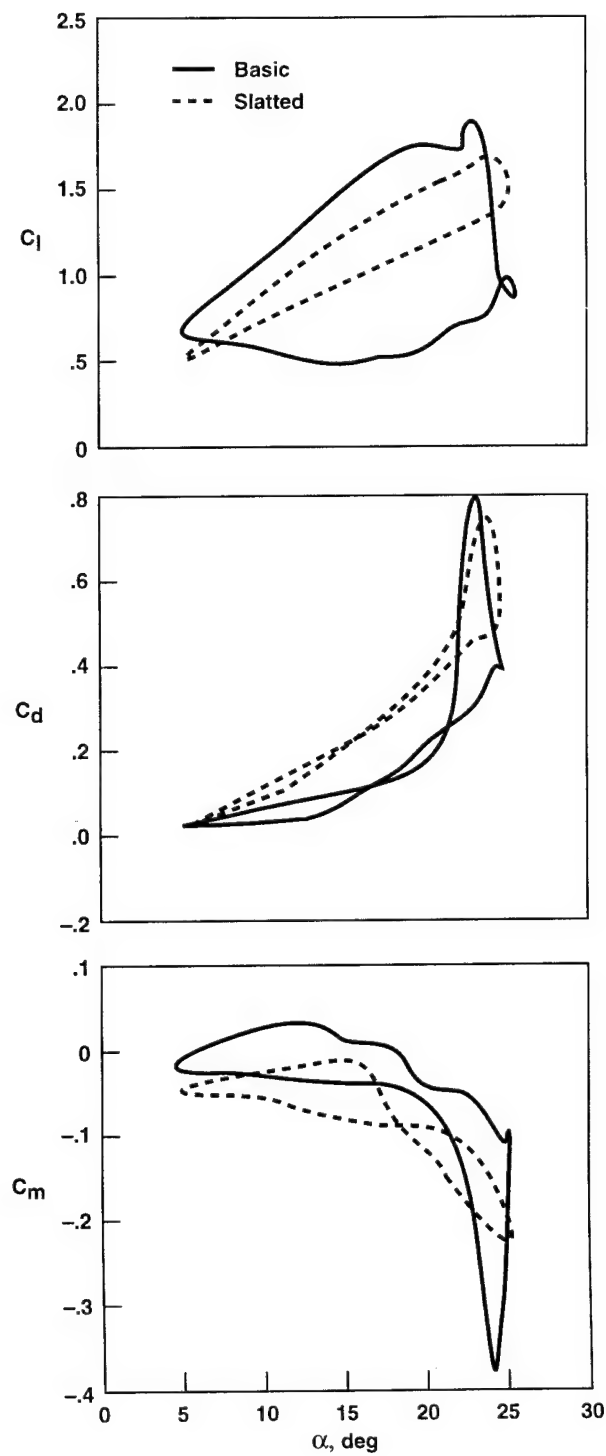


Figure 3. Calculated load-hysteresis loops for the VR-7 airfoil at  $Re = 200,000$  and  $k = 0.1$ .

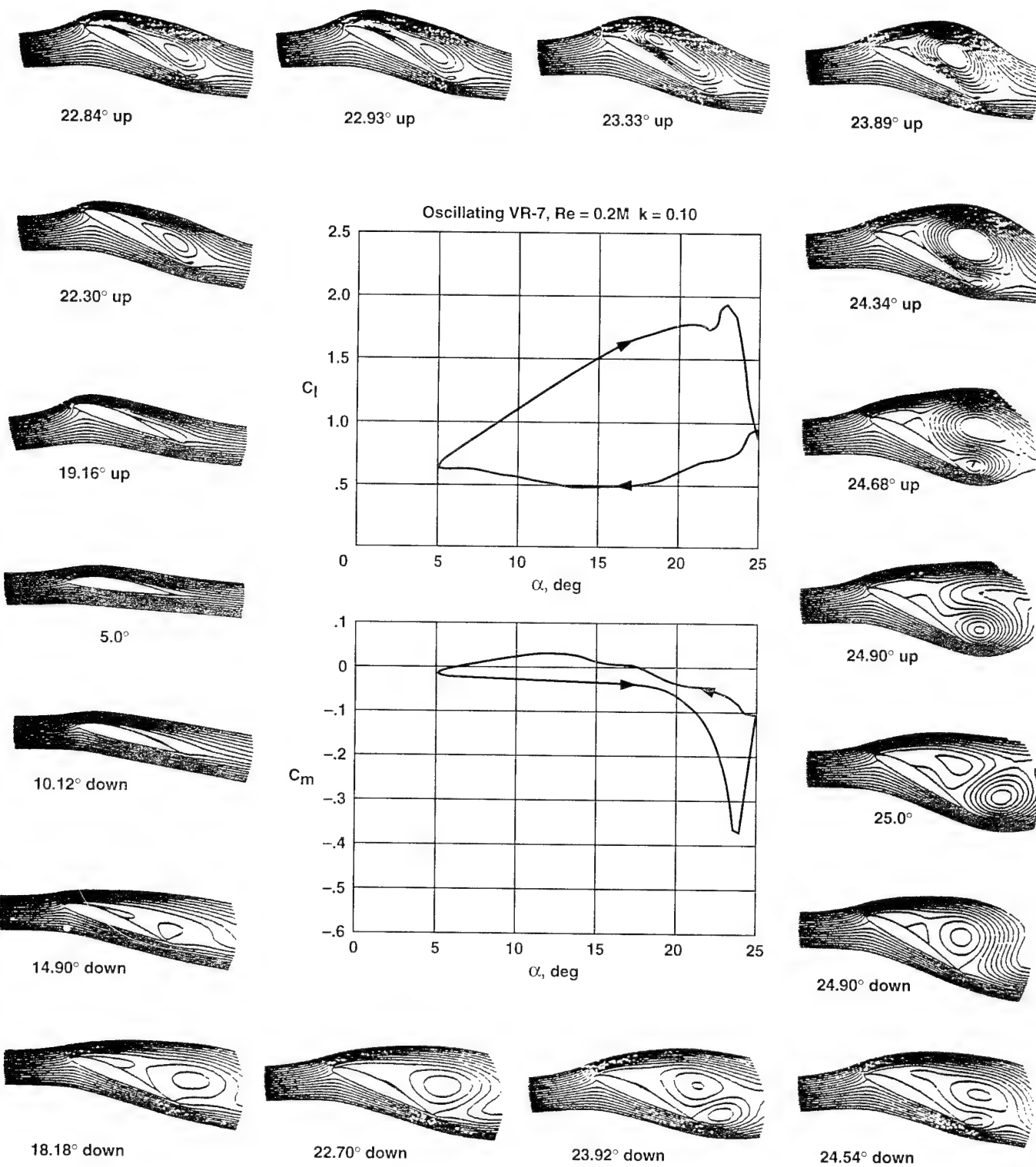


Figure 4. Calculated instantaneous streamlines and load loop for the VR-7 airfoil at  $Re = 200,000$  and  $k = 0.1$ .

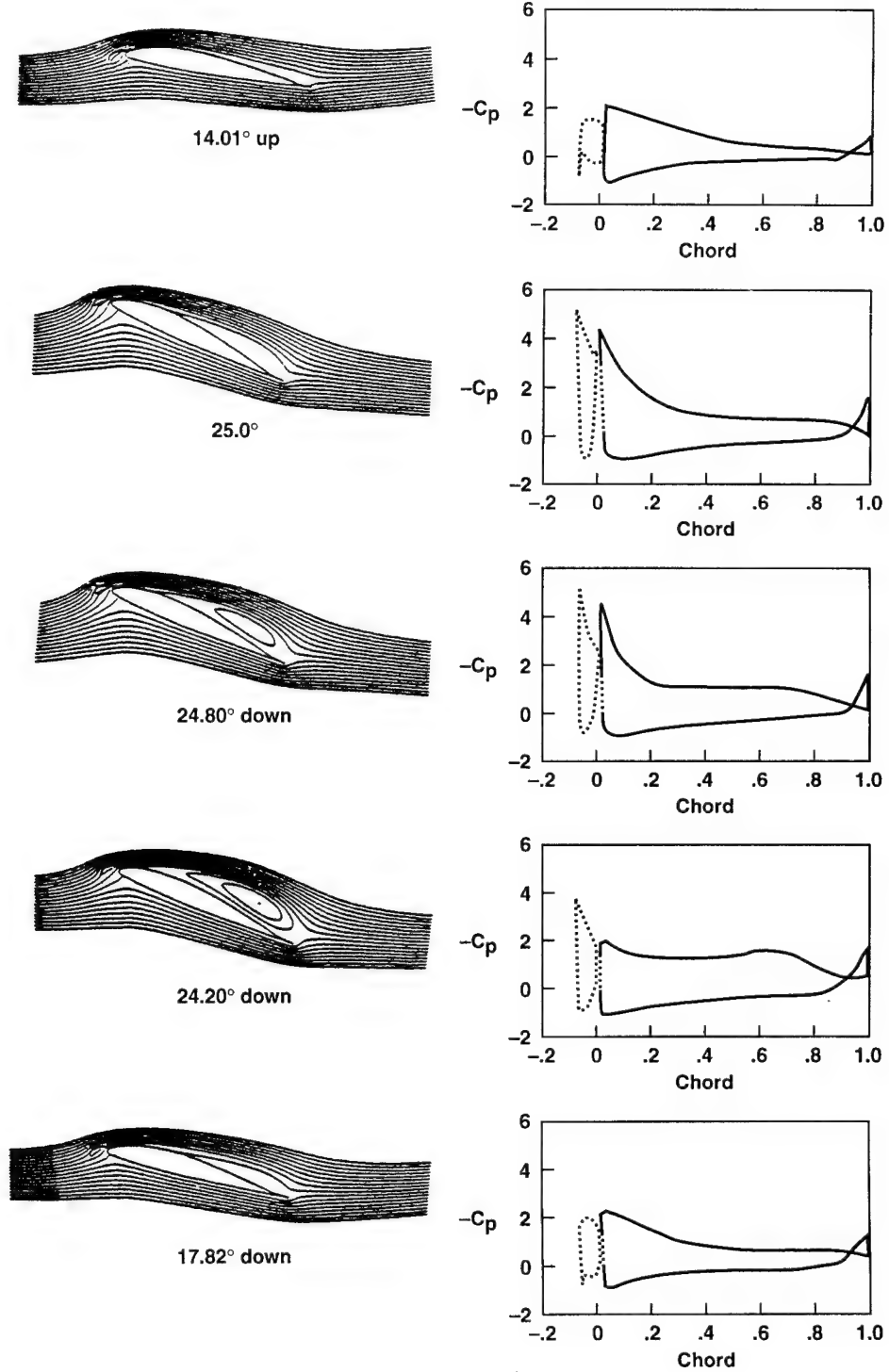


Figure 5. Calculated instantaneous streamlines and surface pressures for the slatted VR-7 airfoil at  $Re = 200,000$  and  $k = 0.1$ .

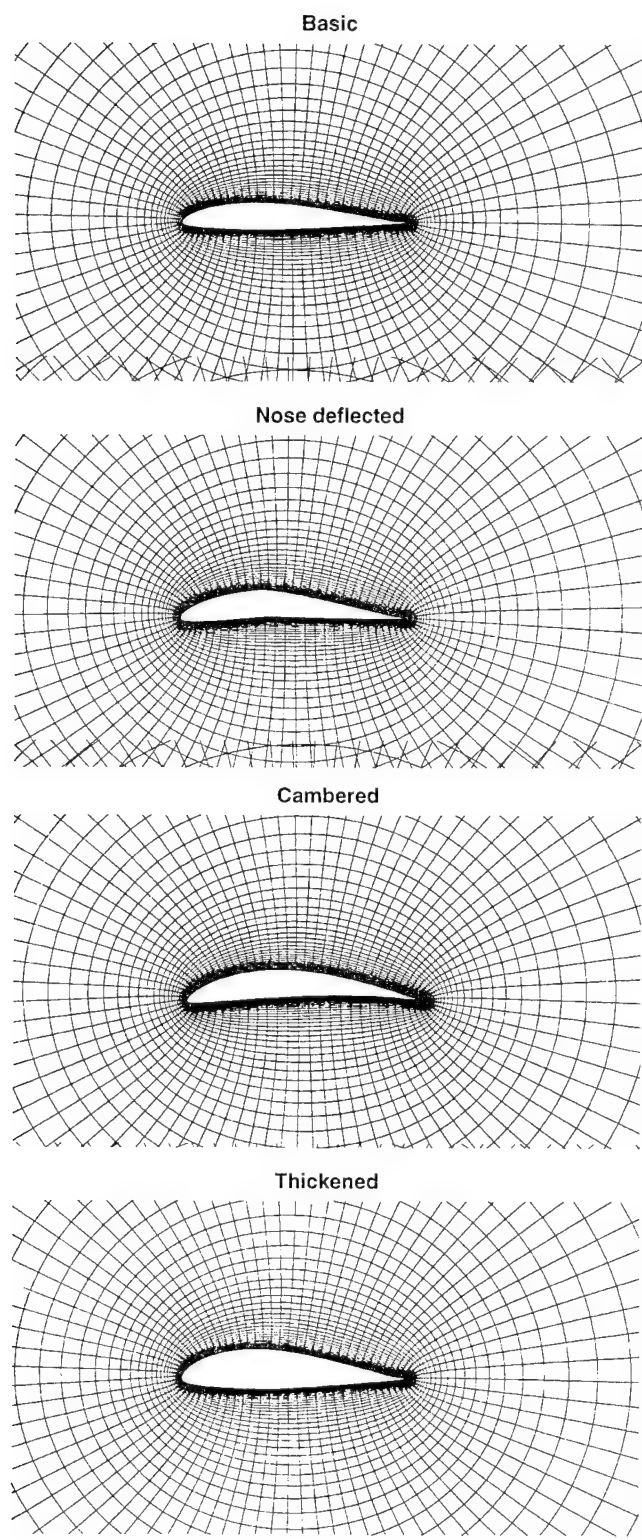


Figure 6. Types of deformable VR-7 airfoils.

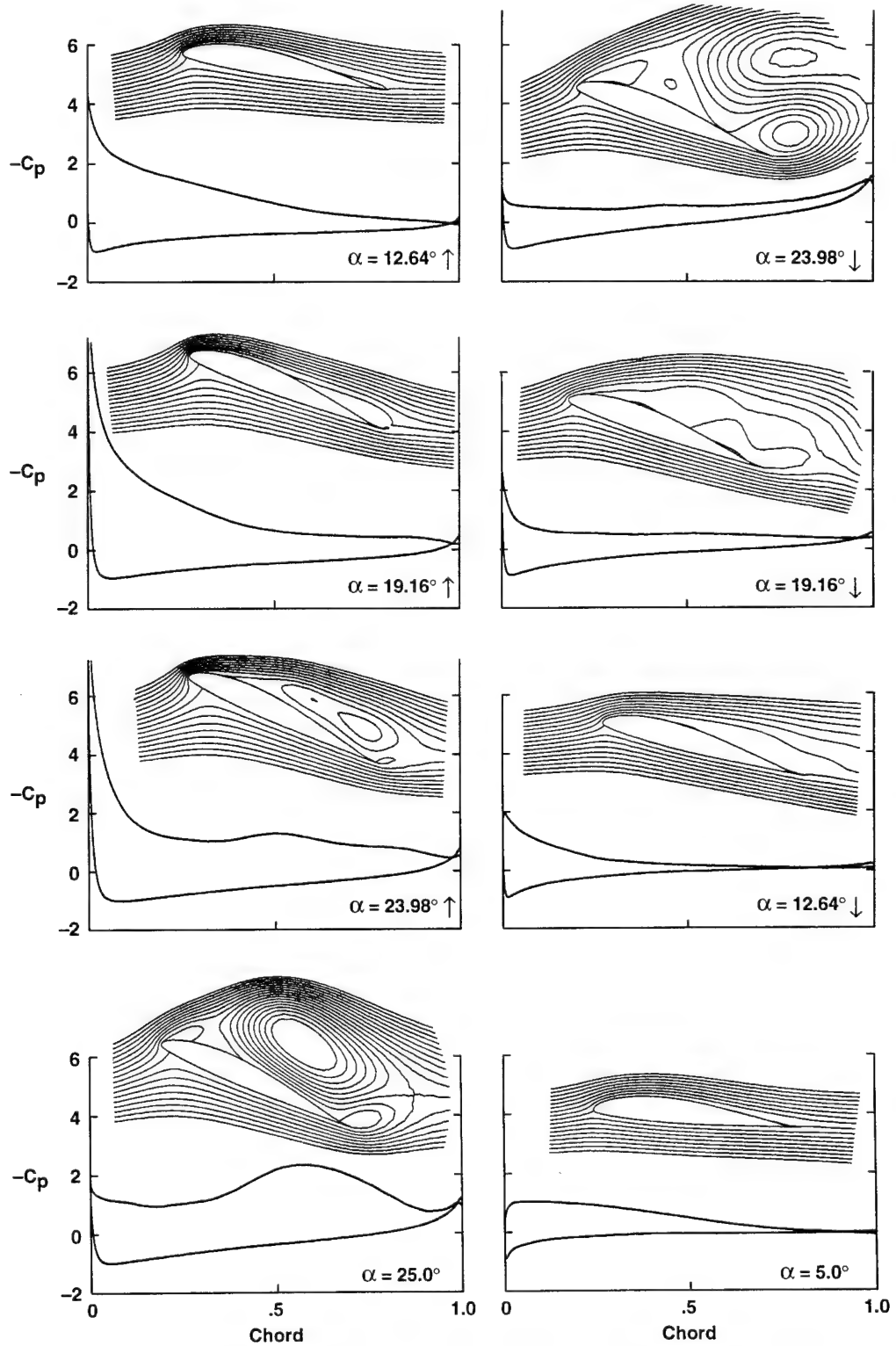


Figure 7. Calculated instantaneous streamlines and surface pressure for the basic VR-7 airfoil at  $Re = 1,000,000$  and  $k = 0.15$ .

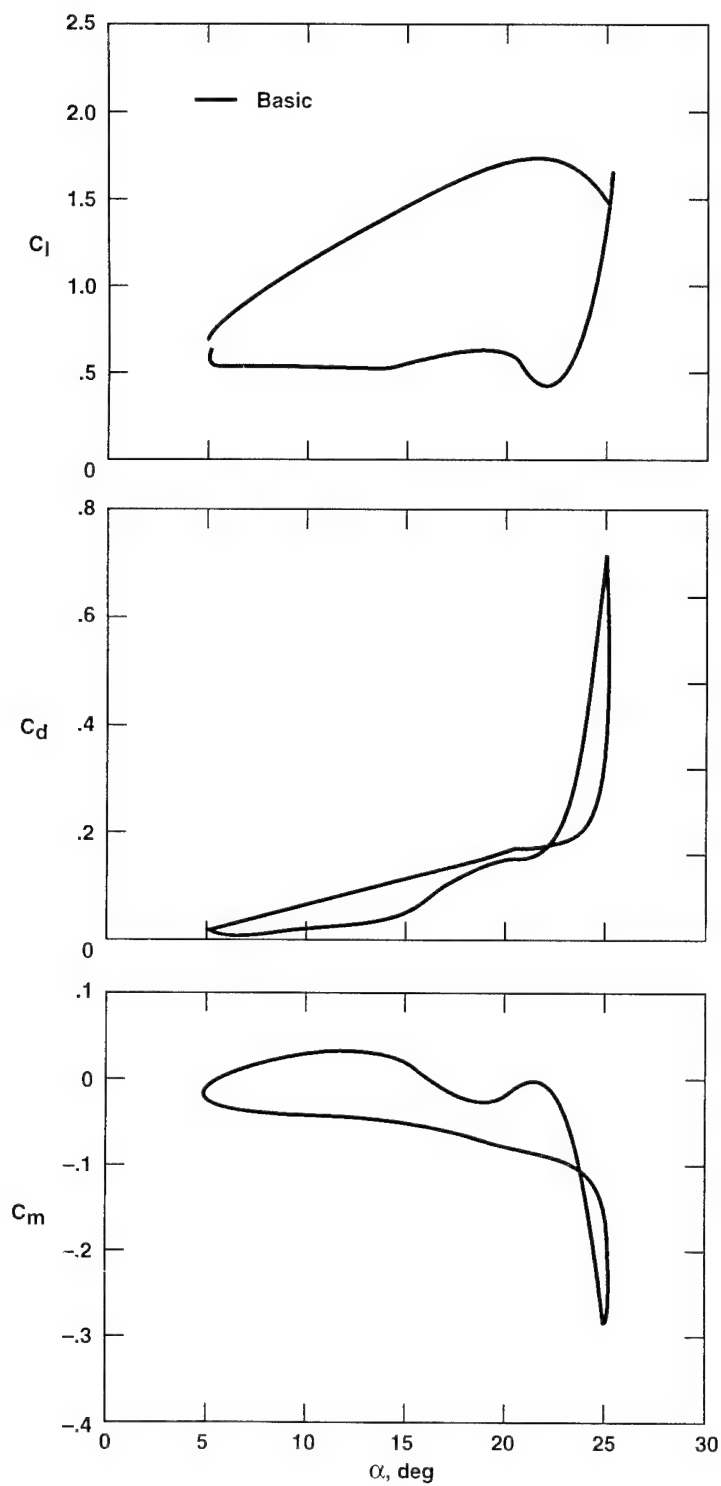


Figure 8. Calculated load-hysteresis loops for the basic VR-7 airfoil at  $Re = 1,000,000$  and  $k = 0.15$ .

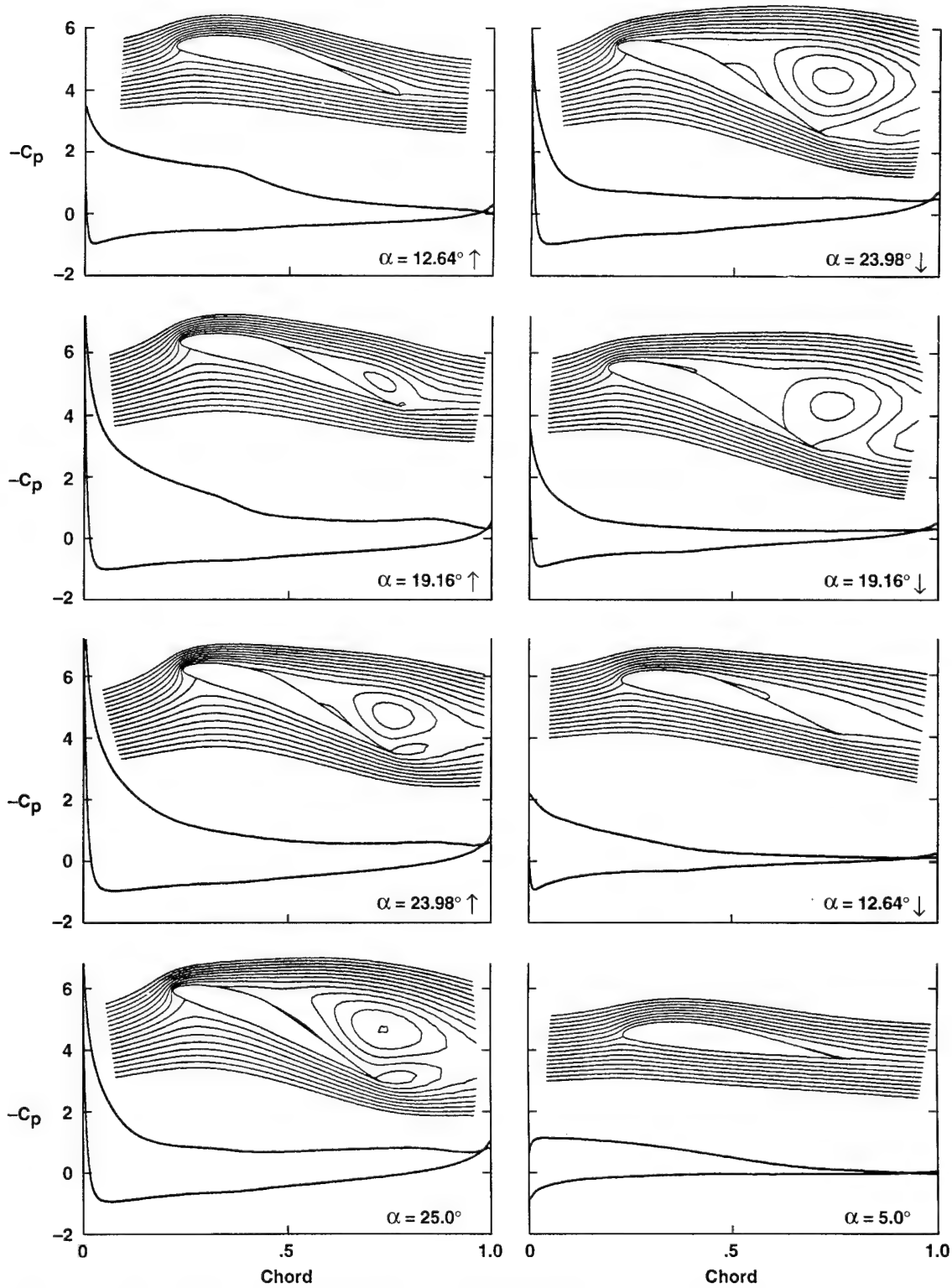


Figure 9. Calculated instantaneous streamlines and surface pressure for the nose-deflected VR -7 airfoil at  $Re = 1,000,000$  and  $k = 0.15$ .

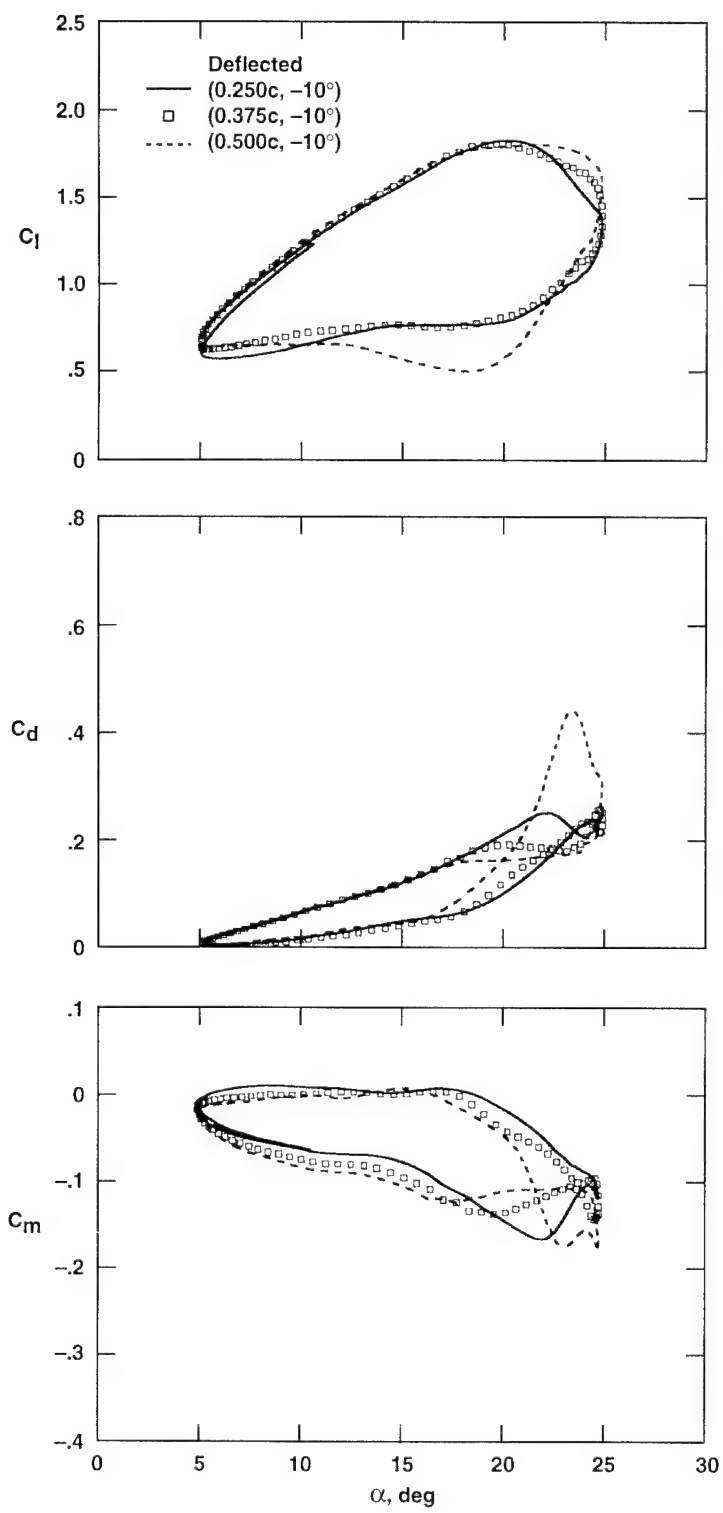


Figure 10. Calculated load-hysteresis loops for the nose-deflected VR-7 airfoil at  $Re = 1,000,000$  and  $k = 0.15$ .

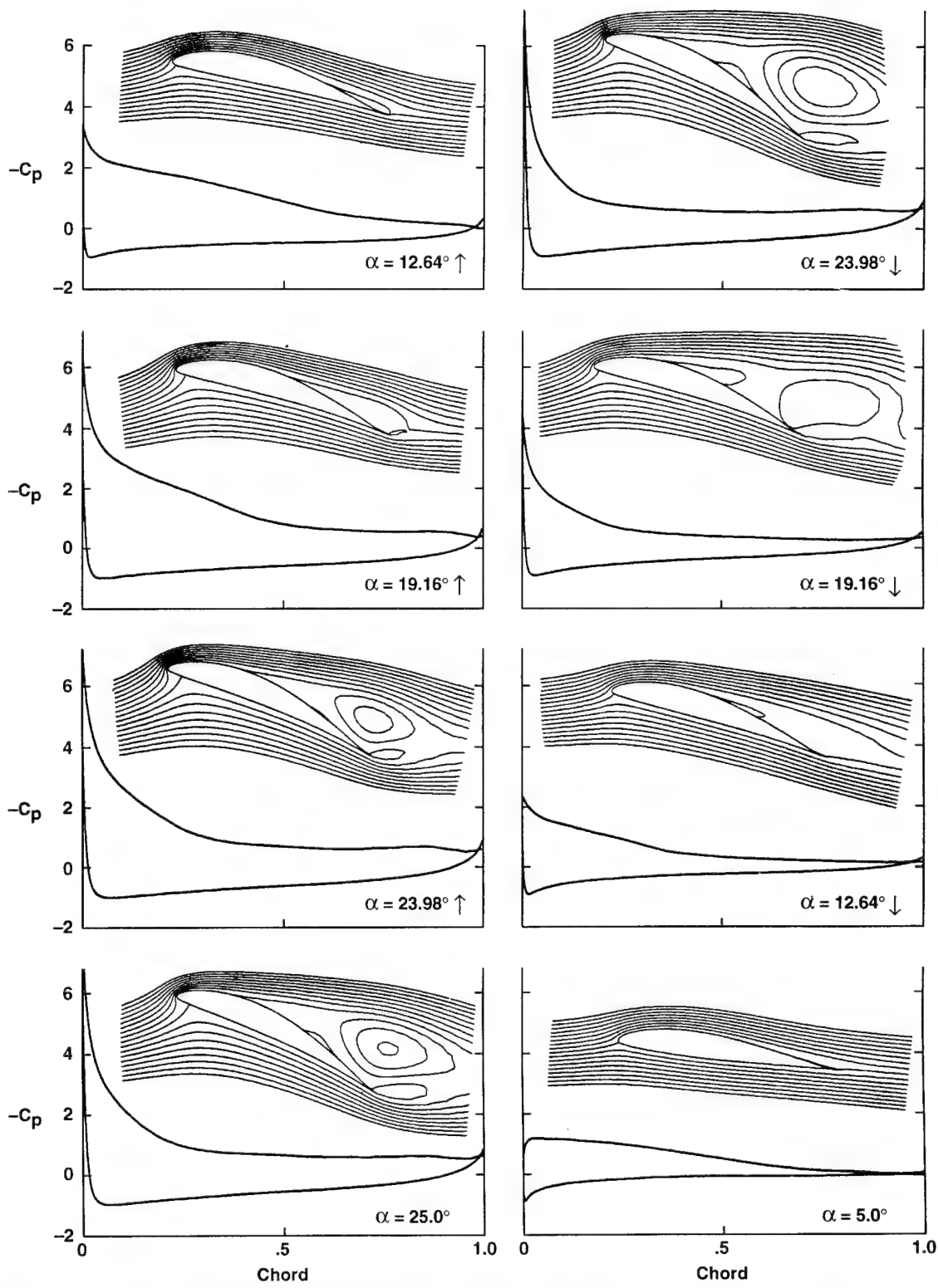


Figure 11. Calculated instantaneous streamlines and surface pressures for the cambered VR-7 airfoil at  $Re = 1,000,000$  and  $k = 0.15$ .

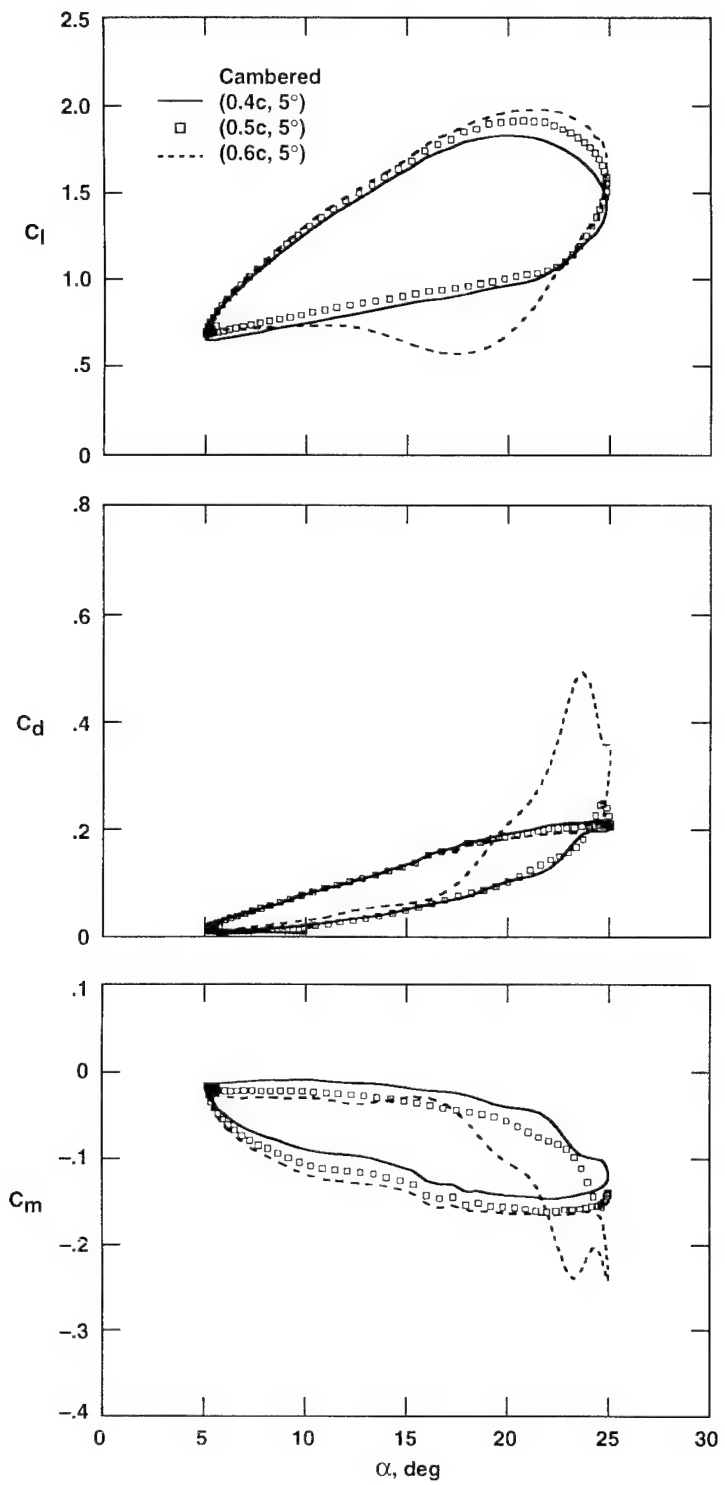


Figure 12. Calculated load-hysteresis loops for the cambered VR-7 airfoil at  $Re = 1,000,000$  and  $k = 0.15$ .

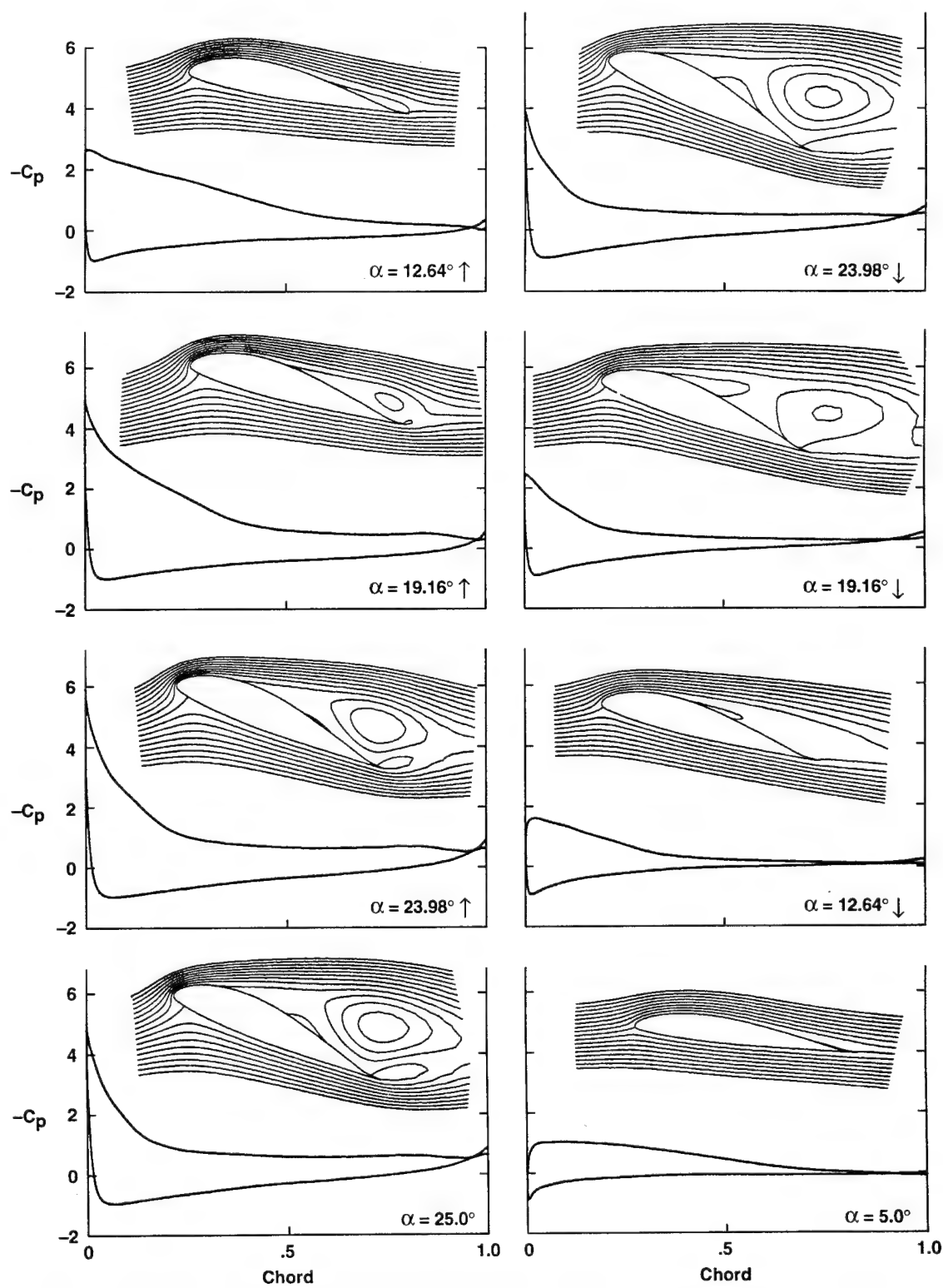


Figure 13. Calculated instantaneous streamlines and surface pressure for the thickened VR-7 airfoil at  $Re = 1,000,000$  and  $k = 0.15$ .

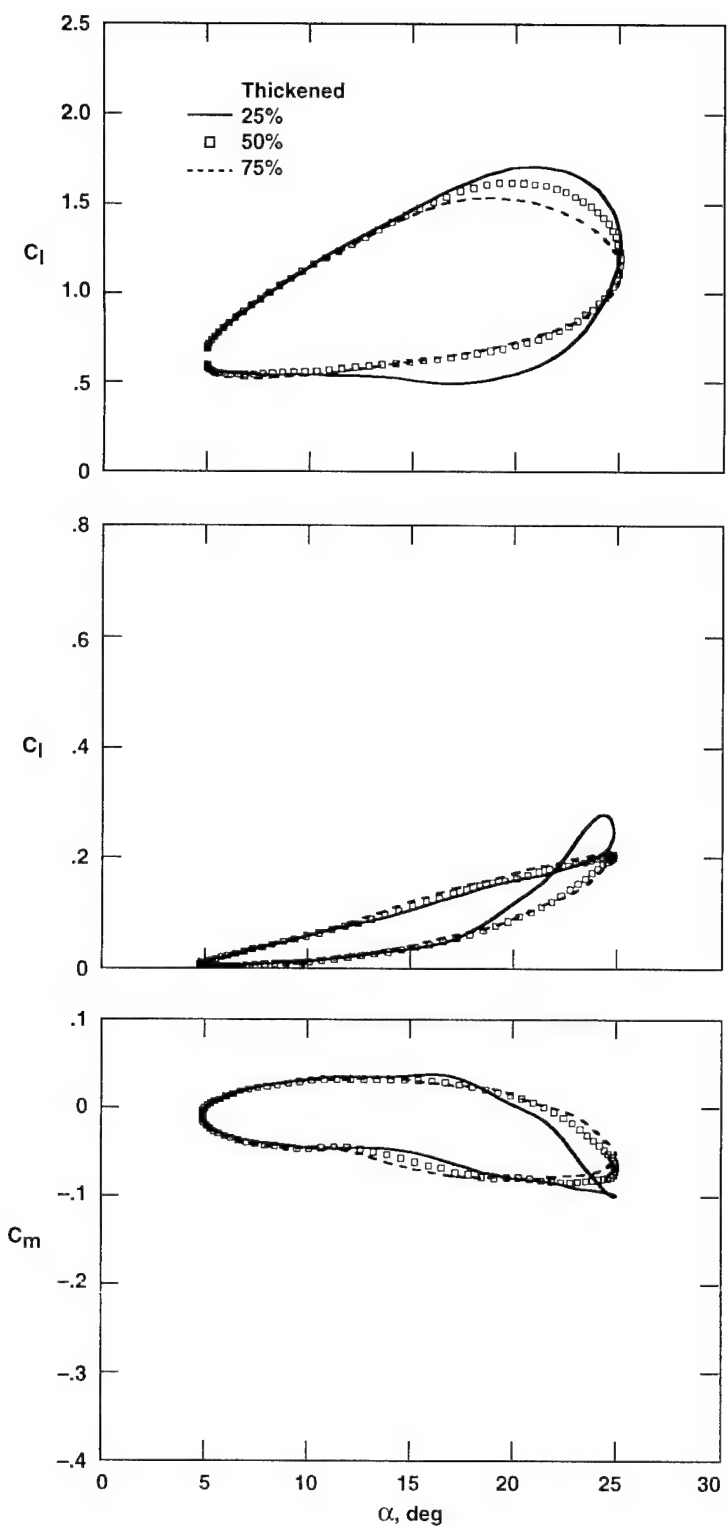


Figure 14. Calculated load-hysteresis loops for the thickened VR-7 airfoil at  $Re = 1,000,000$  and  $k = 0.15$ .

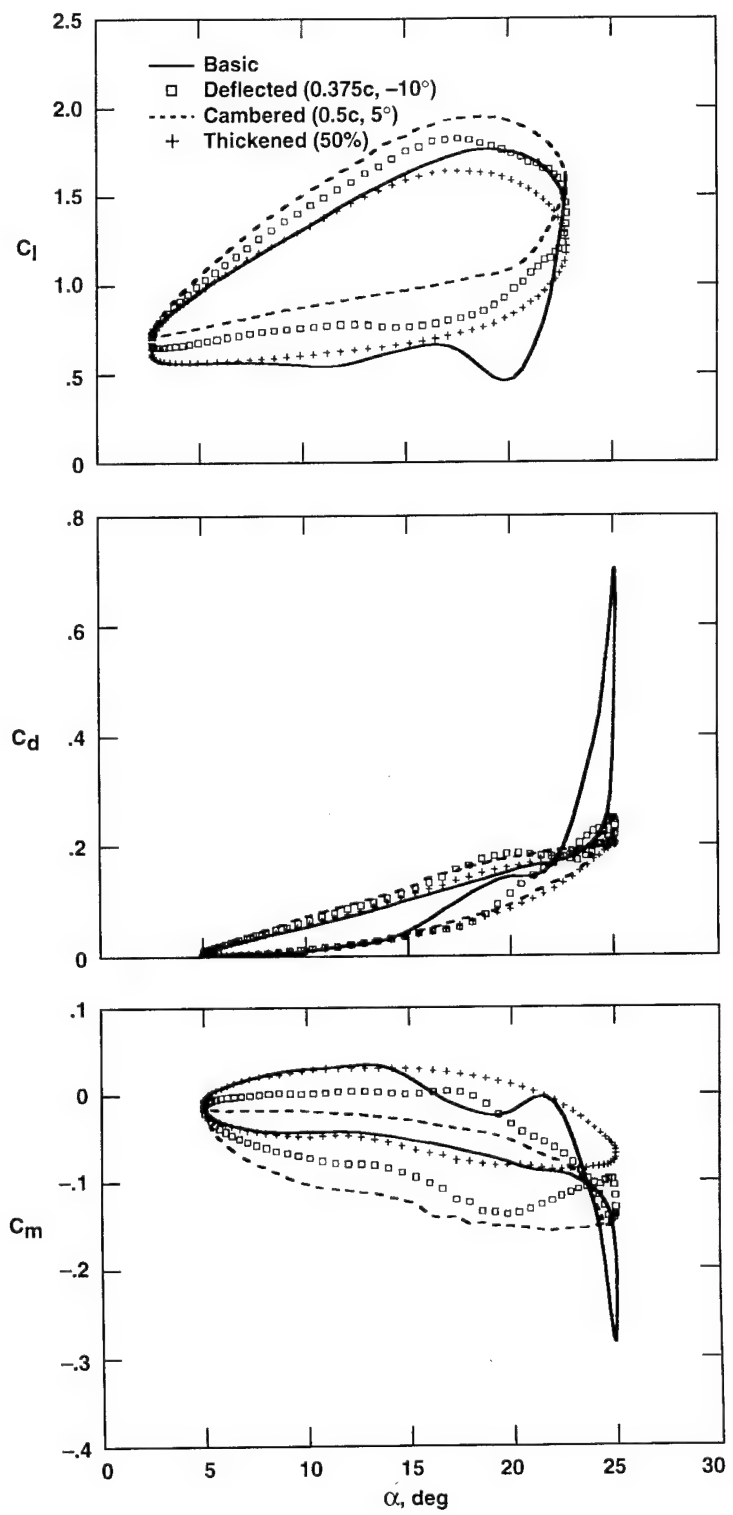


Figure 15. Comparison of calculated load-hysteresis loops for the deformable VR-7 airfoil at  $Re = 1,000,000$  and  $k = 0.15$ .

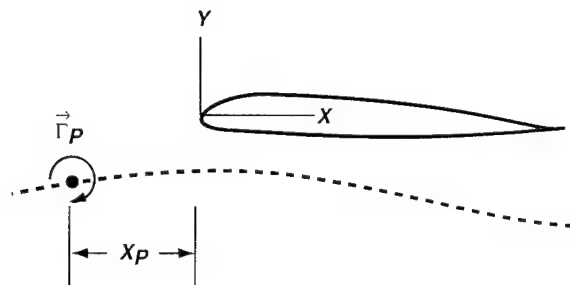


Figure 16. Schematic of vortex–airfoil interaction.

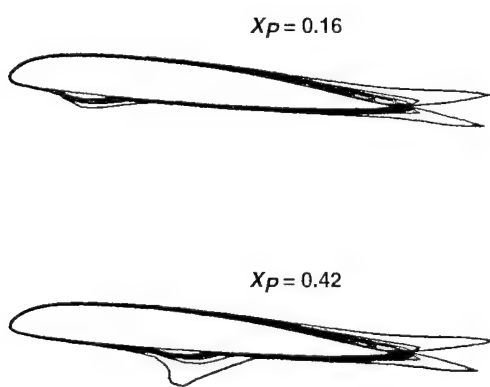


Figure 17. Distributed vorticity contours around basic VR-12 airfoil.

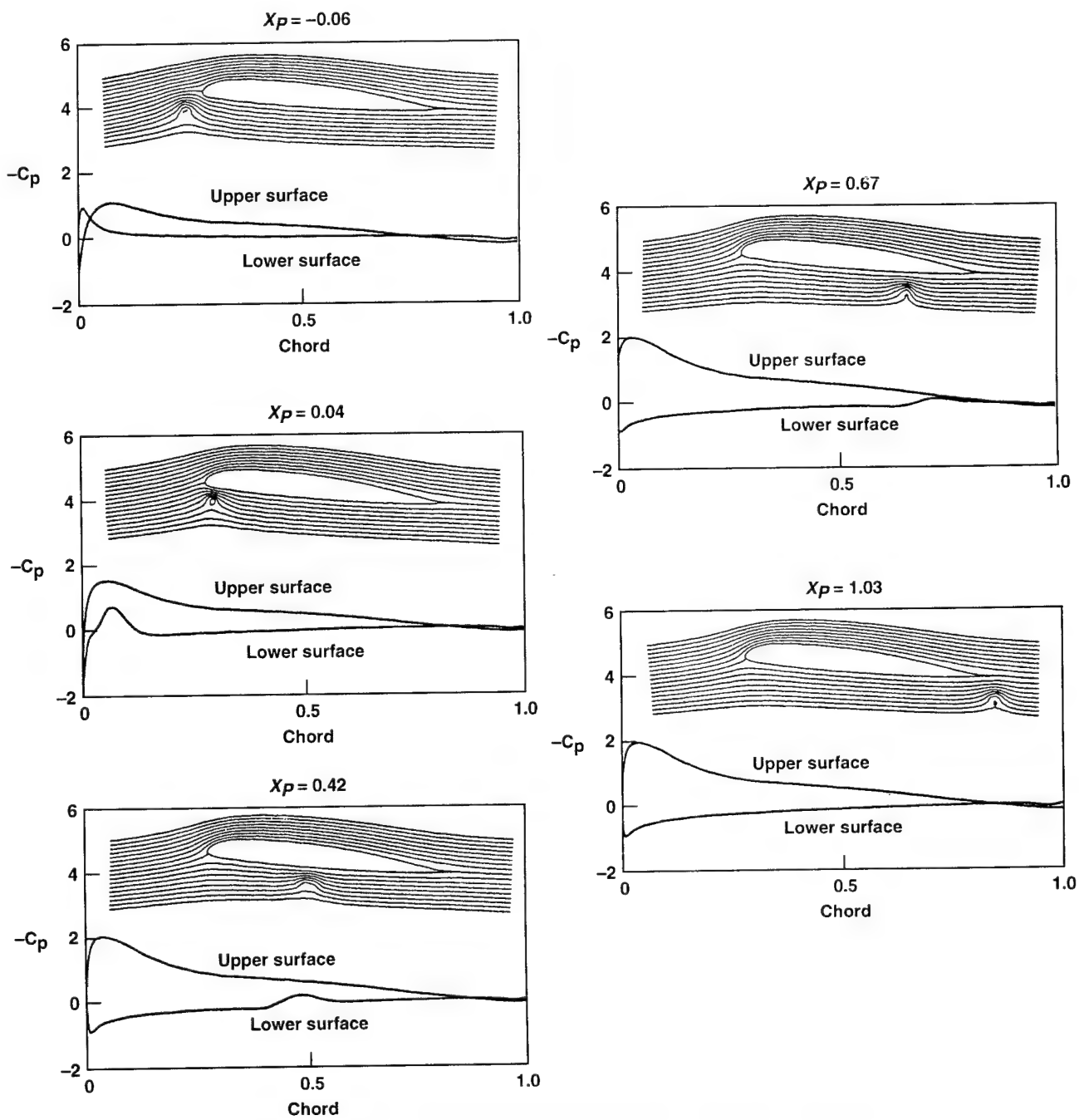


Figure 18. Streamlines and surface pressures during vortex–airfoil interaction for the basic VR-12 airfoil.

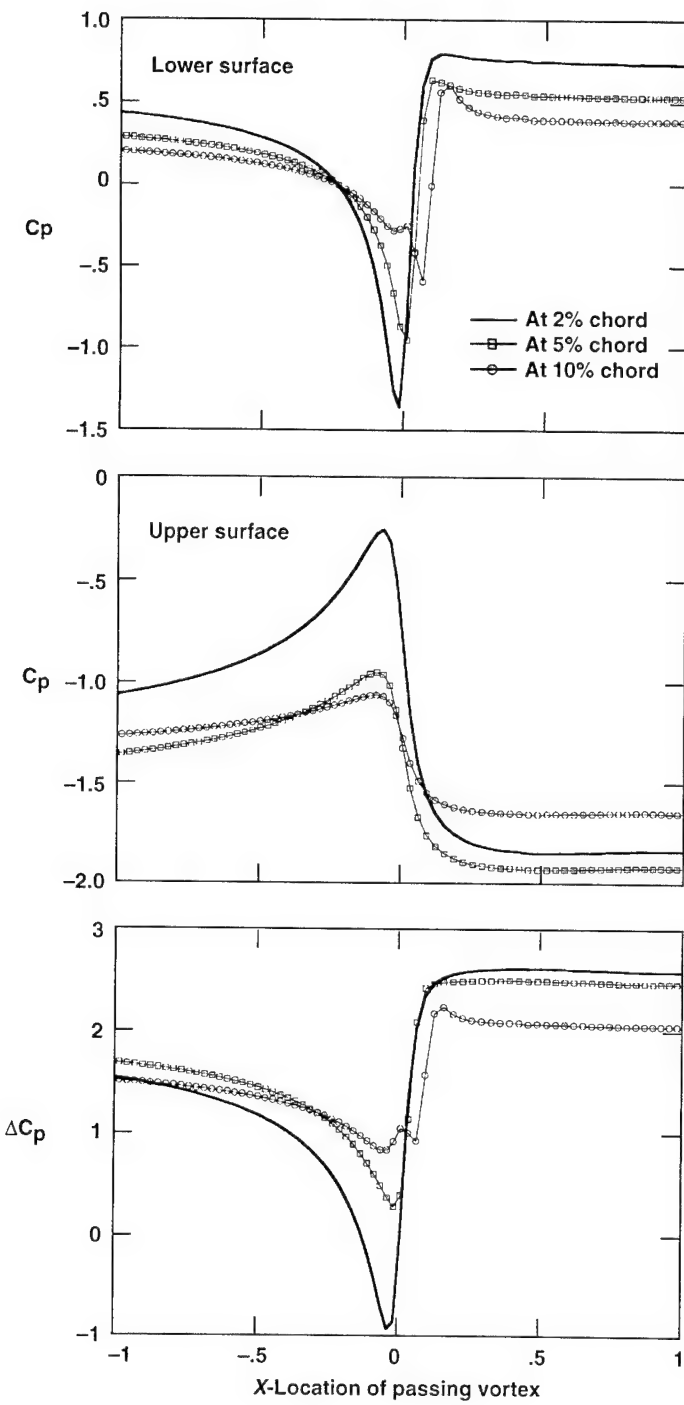


Figure 19. Surface and differential pressures at three chord locations on the basic VR-12 airfoil.

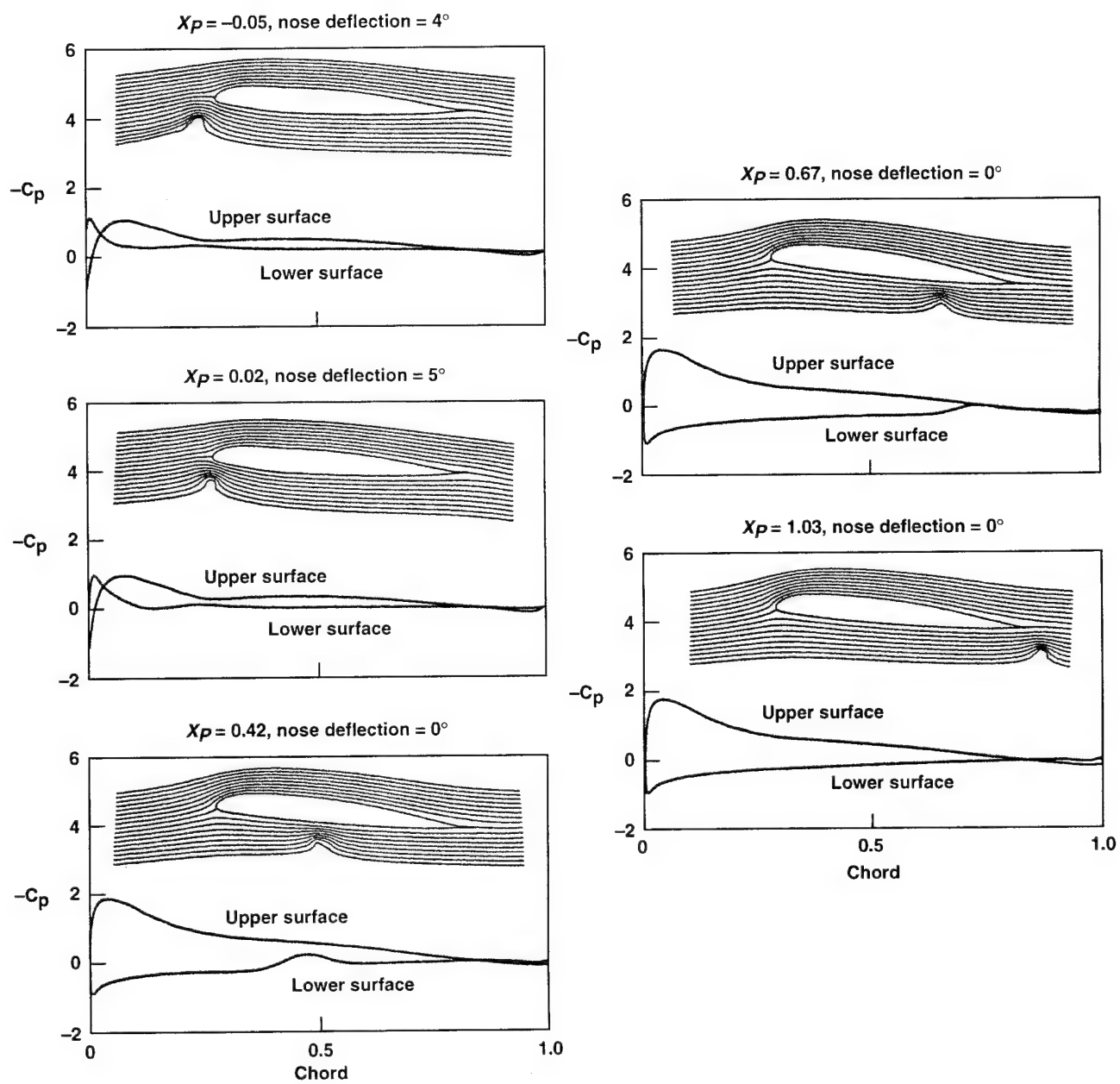


Figure 20. Streamlines and surface pressures during vortex–airfoil interaction for a deforming VR-12 (0.25 c,  $5^\circ$ ) airfoil.

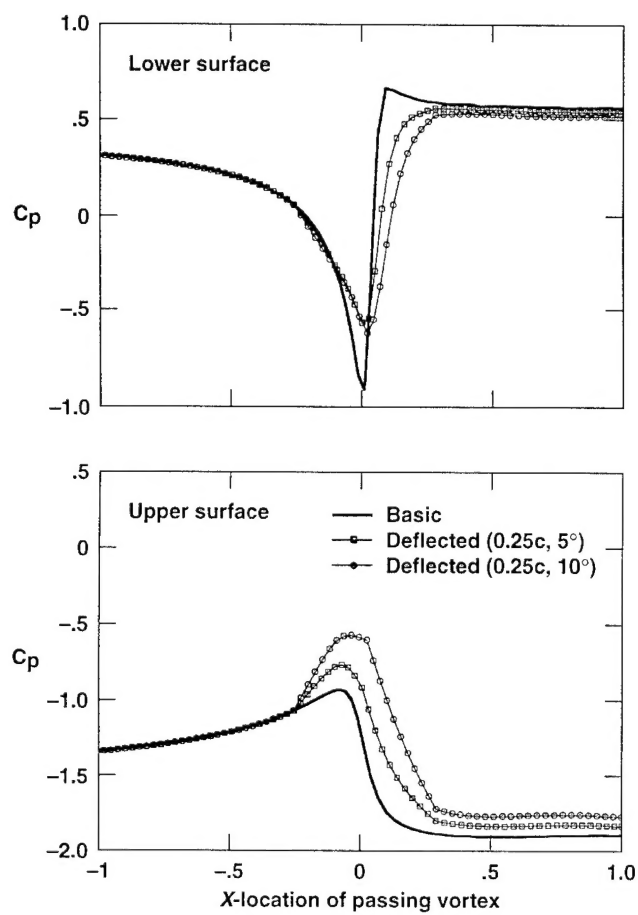


Figure 21. Comparison of pressure fluctuations at 5-percent chord for nose-deflected VR-12 airfoils.

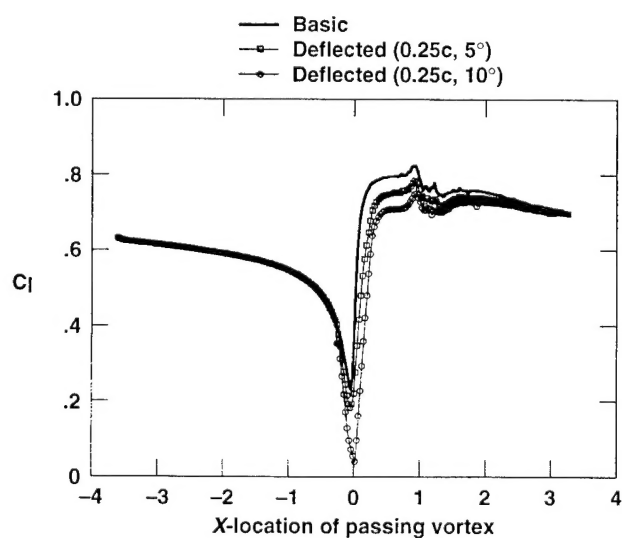
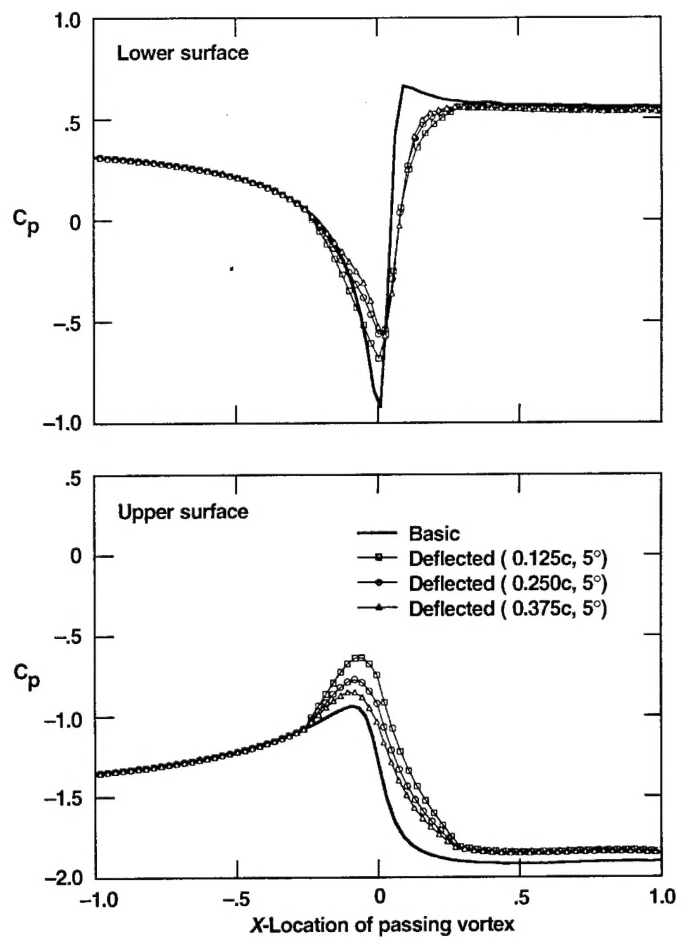


Figure 22. Comparison of lift coefficients for nose-deflected VR-12 airfoils.



*Figure 23. Comparison of surface and differential pressure fluctuations at 5-percent chord for nose-deflected VR-12 airfoils.*

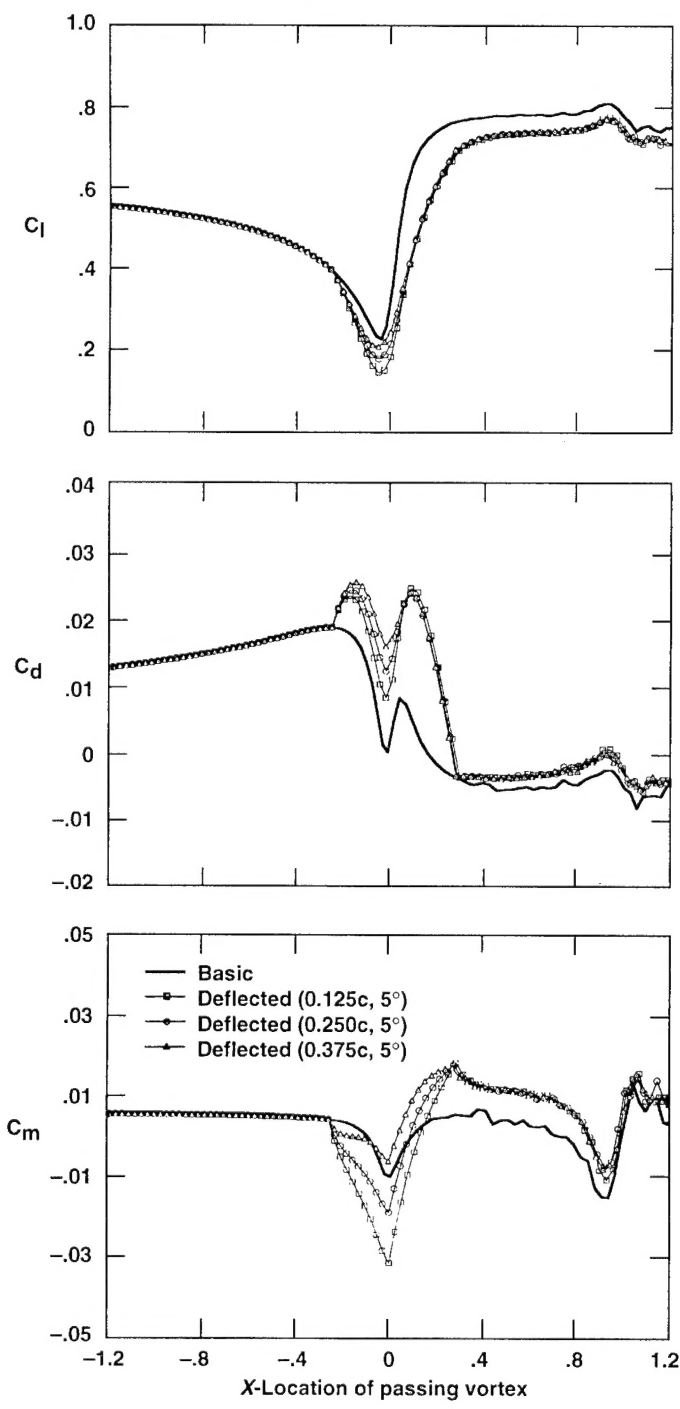


Figure 24. Comparison of aerodynamic loads for nose-deflected VR-12 airfoils.

# REPORT DOCUMENTATION PAGE

*Form Approved  
OMB No. 0704-0188*

Public reporting burden for this collection of information is estimated to average 1 hour per response, including the time for reviewing instructions, searching existing data sources, gathering and maintaining the data needed, and completing and reviewing the collection of information. Send comments regarding this burden estimate or any other aspect of this collection of information, including suggestions for reducing this burden, to Washington Headquarters Services, Directorate for Information Operations and Reports, 1215 Jefferson Davis Highway, Suite 1204, Arlington, VA 22202-4302, and to the Office of Management and Budget, Paperwork Reduction Project (0704-0188), Washington, DC 20503.

<b>1. AGENCY USE ONLY (Leave blank)</b>			<b>2. REPORT DATE</b> July 1995		<b>3. REPORT TYPE AND DATES COVERED</b> Technical Paper	
<b>4. TITLE AND SUBTITLE</b>  ZETA II Code for Determining the Flow Around Multielement and Deformable Airfoils			<b>5. FUNDING NUMBERS</b>  505-59-87			
<b>6. AUTHOR(S)</b>  C. M. Wang,* J. C. Wu,* K. W. McAlister, and C. Tung			<b>8. PERFORMING ORGANIZATION REPORT NUMBER</b>  A-950064			
<b>7. PERFORMING ORGANIZATION NAME(S) AND ADDRESS(ES)</b>  Ames Research Center, Moffett Field, CA 94035-1000 and Aeroflightdynamics Directorate, U.S. Army Aviation and Troop Command, Ames Research Center, Moffett Field, CA 94035-1000  *School of Aerospace Engineering, Georgia Institute of Technology, Atlanta, Georgia			<b>9. SPONSORING/MONITORING AGENCY NAME(S) AND ADDRESS(ES)</b>  National Aeronautics and Space Administration Washington, DC 20546-0001 and U.S. Army Aviation and Troop Command, St. Louis, MO 63120-1798			
<b>10. SPONSORING/MONITORING AGENCY REPORT NUMBER</b>  NASA TP-3567 USAATCOM TR-95-A-004			<b>11. SUPPLEMENTARY NOTES</b>  Point of Contact: Kenneth W. McAlister, Ames Research Center, MS 215-1, Moffett Field, CA 94035-1000; (415) 604-5892			
<b>12a. DISTRIBUTION/AVAILABILITY STATEMENT</b>  Unclassified-Unlimited Subject Category – 02  Available from the NASA Center for AeroSpace Information, 800 Elkrige Landing Road, Linthicum Heights, MD 21090; (301) 621-0390				<b>12b. DISTRIBUTION CODE</b>		
<b>13. ABSTRACT (Maximum 200 words)</b>  <p>The present NASA–University consortium involves research on the development of an efficient and accurate numerical procedure to treat general unsteady viscous flows. Of particular interest in the present work are flows relevant to helicopter rotors. Special efforts are centered on new concepts applied to the rotorblade configuration on the helicopter to improve the rotor aerodynamic characteristics. Among them, airfoil dynamic stall and the aerodynamic noise of vortex–airfoil interactions were extensively studied by using the numerical procedure. The procedure, based on the formulation of an integral representation of the velocity vector and the vorticity transport equation, is used to solve incompressible Navier–Stokes flows. ZETA, a computer code developed at Georgia Tech, is used as the basis for the development of an extended computer code, ZETA II. The ZETA code is very efficient in the treatment of single, solid airfoils undergoing arbitrary motions. The extended ZETA II can treat the two-element airfoil, the deformable airfoil, and vortex–airfoil interaction.</p> <p>New concepts aimed at improving the helicopter maneuverability and susceptibility are studied, including the slatted airfoil and the deformable airfoil. Numerical results obtained by using the ZETA II code show that both slatted and deformable airfoils reduce the dynamic stall and that the deformable airfoil reduces the blade–vortex interaction (BVI) noise.</p>						
<b>14. SUBJECT TERMS</b>  Multielement airfoils, Deforming airfoils, High performance				<b>15. NUMBER OF PAGES</b> 46		
				<b>16. PRICE CODE</b> A03		
<b>17. SECURITY CLASSIFICATION OF REPORT</b> Unclassified		<b>18. SECURITY CLASSIFICATION OF THIS PAGE</b> Unclassified		<b>19. SECURITY CLASSIFICATION OF ABSTRACT</b>		
				<b>20. LIMITATION OF ABSTRACT</b>		